J. Indian Inst. Sci., Jan–Feb. 1990, **70**, 29–73.

IISc THESES ABSTRACTS

Thesis Abstract (Ph.D.)

Surface ray tracing on convex quadrics with applications to mutual coupling between antennas on aerospace bodies by Rakesh Mohan Jha.
Research supervisors: N. Balakrishnan and P. R. Mahapatra.
Department: Aerospace Engineering.

1. Introduction

The basis of most modern high-frequency ray-theoretic methods is the Geometric Theory of Diffraction (GTD), which is based on the computation of the diffraction coefficients[1]. These coefficients depend on the nature of the surface of the scatterer, including its geometric properties. An important step in the ray-theoretic approaches, such as the GTD and its more widely used extensions like the Uniform Theory of Diffraction (UTD), is the process of ray tracing, consisting of the determination of the surface-, edge- and tip-diffracted ray paths in accordance with the extended Fermat's principle[2].

Although an accurate analytical approach to the high-frequency antenna mutual coupling analysis has clear advantages, the present capability in this direction is restricted to simple shapes such as circular cylinder and cone[3], and sphere[2]. A few other quadrics such as the ellipsoids have been treated only for special cases of conveniently located slot antennas, effectively reducing them to two-dimensional problems.

The work presented in the thesis is concerned with the generalized solution of surface ray-tracing problems associated with both 'simple' as well as hybrid surfaces of the type encountered in aerospace vehicles and satellites. The primary motivation for this work comes from the practical need to develop a comprehensive theoretical approach to the high-frequency analysis of mutual coupling between antennas mounted on realistic aerospace structures.

2. Analytical surface generation

A vast majority of aerospace structures can be conveniently modeled as combinations of simpler quadric surfaces. The quadrics most commonly encountered among the aerospace shapes are the quadric cylinders (QUACYLs) and the quadric surfaces of revolution (QUASORs). The complete class of QUACYLs consists of circular, elliptic, hyperbolic and parabolic cylinders. Similarly, the right circular cone, sphere, ellipsoid, and the hyperboloid and paraboloid of revolution constitute the non-degenerate class of QUASORs. These QUACYLs and QUASORs are recognized as the coordinate surfaces of the appropriate Eisenhart Coordinate Systems[4]. The term 'Eisenhart Coordinate System' refers to the eleven first and second degree orthogonal curvilinear coordinate systems of Eisenhart.

3. Overview of the work

The problem of high-frequency mutual coupling between antennas on aerospace bodies underlines the need for a systematic approach to ray tracing over convex scatterers. An overview of the current methods in numerical electromagnetics is presented and the importance of ray tracing is emphasized for the high-frequency methods. Since ray tracing is applied in several diverse areas, a survey of the ray-tracing techniques employed in those areas is carried out with an objective to determine their applicability in EM theory.

A generalized approach to the analytical ray tracing has been developed in this thesis. This approach, based on the geodesic coordinate system in differential geometry, is quite general and can be applied to a wide class of convex bodies.

The power of this technique stems from the use of Eisenhart coordinate systems which facilitate the description of relatively complex convex shapes by holding one of the orthogonal coordinate parameters constant. Through the introduction of a 'shaping parameter' in the mathematical analysis, such a depiction also enables modeling of a wide variety of practical shapes, in terms of flatness/sharpness, while using only a limited number of generic surface shapes such as cones, cylinders, ellipsoids and paraboloids.

The canonical shapes considered include both developable and non-developable surfaces. The surface ray geometric parameters required in the UTD mutual coupling computations for the QUACYLs (with general parabolic cylinder (GPCYL), as a specific example) are derived in the closed form. Similarly, an exhaustive treatment is presented for the ray geometric parameters for the more complex case of QUASORs, with general paraboloid of revolution (GPOR) as an example. The expressions are derived in one-parameter form, requiring only a simple univariate numerical search. These original results have led to the explicit determination of mutual coupling between antennas over the quadric convex surfaces, in general.

A surface modeling paradigm has been systematically constructed in the thesis. As a logical step after ray tracing over the canonical quadric shapes (*i.e.*, individual QUACYLs and QUASORs), hybrid structures of practical interest are considered. Included in this class is the aircraft wing modeled as a hybrid QUACYL as a combination of matched circular and general parabolic cylindrical segments. For this structure, the ray parameters have been obtained in closed form.

The paradigm also facilitates the treatment of the more complex case of the hybrid QUASORs such as a non-developable satellite launch vehicle (SLV) modeled by matched sections of GPOR and circular cylinder. The ray geometric parameters have been obtained for such a case in the quasi-analytical form. This problem has been rendered tractable by the introduction of the Hertz's principle of particle dynamics into the field of ray-theoretic analysis.

Explicit and exhaustive determination of the effects of the geodesics of all orders on the generalized surfaces has yielded a clear insight into the contribution due to different geodesics. This has also led to the discovery of situations where the highest order of geodesics, contrary to the earlier belief, is finite.

The power of the approach, employed in the thesis, is re-emphasized by the ease of its applicability to even non-Eisenhart surfaces such as an ogive, for which most of the ray parameters are obtained. In the concluding chapter, the ideas for extensions of the concepts developed in the thesis, have been outlined, as suggestions for future work.

Although the immediate motivation for the work reported in the thesis comes from aerospace applications, the work is of a far more general nature, with direct applications in widely diverse areas. For example, the methods developed in this thesis could be highly relevant to the modern discipline of

computer graphics, especially in the areas of computer surface generation (CSG), lighting model, texture modeling and soft shadow generation, which depend on ray-tracing algorithms extensively.

References

1. KELLER, J. B. Geometrical theory of diffraction, *J. Opt. Soc. Am.*, 1962, **52**, 116–130.
2. PATHAK, P. H. AND WANG, N. Ray analysis of mutual coupling between antennas on a convex surface, *IEEE Trans.*, 1981, **AP-29**, 911–922.
3. LEE, S. W. A review of GTD calculation of mutual admittance of slot conformal array, *Electromagnetics*, 1982, **2**, 85–127.
4. MOON, P. AND SPENCER, D. E. *Field theory handbook*, 1971, Springer-Verlag.

Thesis Abstract (Ph.D.)

Maximum likelihood parameter estimation method for a class of nonlinear systems and its applications to problems in flight mechanics by R. V. Jategaonkar.
Research supervisors: U. R. Prasad and S. Balakrishna (NAL).
Department: School of Automation.

1. Introduction

Equations of motion with constant coefficients linearized at a particular reference equilibrium state of a flight vehicle have been used in the past to determine the aircraft parameters, such as stability and control derivatives. System identification methods have provided convenient means during the last two decades to generate, in majority of cases, such linear aircraft mathematical models from experimental flight test data. Simplified linear mathematical models have been found to be generally adequate for conventional aircraft and for attached, symmetric flow conditions, which are typical of flights at low angles of attack.

However, the demands of improved manoeuverability in terms of higher angles of attack, higher angular rates and accelerations are continuously increasing. Such high performance characteristics made possible by the advent of active control technology and fly-by-wire concepts, require modern aircraft to fly in extreme flight regimes or to perform large amplitude manoeuvers, or to execute complex coupled motion. Under such flight conditions, diverse aerodynamic phenomena such as flow separation, asymmetric flow, interferences and vortex breakdown which are characterized by their strong nonlinear dependence on the aircraft motion are likely to be induced.

For example, large amplitude manoeuvers can result in longitudinal and lateral mode coupling. At high angles of attack, rolling and yawing moments are found to be nonlinear functions of sideslip angle. Asymmetric breakdown of vortices can lead to aerodynamic hysteresis. In all such cases nonlinear mathematical models have to be invariably postulated to explain the resultant aircraft motion. Validation of such nonlinear postulates using experimental data still remains an unexplored research area.

Whereas nonlinear aircraft models are required to explain the above extreme flight mechanical behaviour, such representations are also essential to generate accurate mathematical models required for optimum tuning of contemporary fly-by-wire aircraft control systems. Apart from the dominant

influences of aircraft dynamic stability parameters, the effects of other nonlinearities in control elements such as deadband, hysteresis, and also time delays play an important role in the overall performance.

Generation of accurate and reliable nonlinear aircraft models is thus of paramount importance both in flight mechanics as well as in control engineering. However, whereas the system identification techniques are well established for linear system models, applications to nonlinear systems have been very restricted. Only a few very specific applications with many practical limitations have so far been reported in the literature. This is mainly because it is, both algorithmically and numerically, very difficult to develop a generalized estimation procedure which can conveniently handle a wide variety of nonlinear model structures.

The research topic envisaged for this dissertation work is to develop, a much desirable, efficient and flexible estimation procedure for a class of nonlinear systems. Computationally attractive and easy-to-implement procedure is considered to be a practical requirement to analyse a wide variety of different flight mechanical phenomena in a routine manner.

2. Parameter estimation method

A general estimation procedure formulated in this thesis is based on the maximum likelihood (ML) principle to determine, from input-output data, the unknown parameters of a dynamical system. The procedure is applicable to system models which may be nonlinear in state and/or control variables as well as in the parameters to be estimated. The nonlinearities may be of continuous or discontinuous types and either single or multivalued.

The optimization problem has been solved using two different techniques. Both the methods yield estimation procedures which retain the several desirable statistical properties associated with the ML estimator. In the first approach, direct optimization of the likelihood function is carried out using minimum search methods[1]. In the second approach, the quasi-linearization method is suitably extended to overcome the generic difficulties associated with such a formulation. In this thesis, the sensitivity coefficients required in the optimization of the log likelihood function are estimated by a numerical procedure considering small parameter perturbations. This eliminates the need for explicit solution of analytically derived complex sensitivity equations.

The two alternative approaches proposed to obtain ML estimates from nonlinear dynamical system models are critically evaluated for their efficiency and numerical performance. Comparative study, based on the estimation results from flight test data using three different models, demonstrate that the quasi-linearization method in which the need for deriving explicit sensitivity equations has been eliminated leads to a practical implementation of a general estimation algorithm. Using this approach an efficient and flexible generalized estimation algorithm for nonlinear systems without requiring additional cumbersome system-dependent programming efforts has been developed. Versatility of this powerful package is demonstrated by analysing four characteristically different parameter estimation problems in the field of flight mechanics.

3. Applications to problems in flight mechanics

The first application considered is that of compatibility checking of aircraft flight test data. The nonlinear kinematical equations of aircraft motion are used to bootstrap the data information through a numerical procedure. Direct applicability of the estimation algorithm developed in this thesis is demonstrated to solve the combined problem of estimating the states, and instrument errors. Specific results obtained for the actual flight test data by considering six degrees-of-freedom

kinematical relations as well as from simplified equations for the longitudinal mode are presented. It is shown that data checking as a preprocessing step is important in the overall analysis and provides valuable information about the quality of flight data recorded.

The second application considered is that of estimating from the flight test data the lift, drag and pitching moment coefficients of an aircraft. Two models are postulated for parameter estimation: i) Conventional linear mathematical model with dimensional derivatives and ii) nonlinear model directly in terms of non-dimensional coefficients with dynamic pressure as an additional variable. The analysis clearly indicates that the nonlinear model yields significantly improved estimation results both qualitatively and quantitatively. Investigations are aimed at evaluating the effects of small changes in flap position on the longitudinal aircraft coefficients through a series of flight experiments at a typical flight condition.

Twelve sets of flight data have been analysed. The results of parameter estimation using a nonlinear model are summarized in Table I. These non-dimensional coefficients C_x and C_z estimated directly are further transformed into lift and drag coefficients C_L and C_D. A plot of lift coefficient C_L as a function of angle of attack α and flap deflection δ_f is shown in fig. 1. The parameter estimation results shown by ● and ▲ symbols agree well with the manufacturer's data shown by continuous lines. Furthermore, the movement of the lift curve with increase in flap deflection is also predicted consistently. It is to be realised here that the lift and drag data have been generated as a Taylor series sum of the individual estimated stability derivatives.

Apart from the above applications to the two classical problems in flight mechanics, new application possibilities of nonlinear ML estimation procedure to dynamical systems with certain specific single and multivalued discontinuous nonlinearties have been demonstrated[2]. Both mechanical and aerodynamic nonlinearities of this kind are investigated. Parametric estimation approach is initially validated by estimating the parameters of nonlinearities such as hysteresis and combined deadband plus saturation using simulated data. The procedure is then applied to a practical problem of identifying, from flight test data, the unknown nonlinear effects in the control surface actuator system of an aircraft.

The fourth problem addressed is the parameter estimation of aerodynamic nonlinearities which induce characteristically different nonlinear aircraft motion of uncommanded sustained roll oscillations. After a brief review of physics of this particular nonlinear flight mechanical phenomenon, the estimation procedure is successfully applied to identify, from simulated aircraft responses, the cubic and hysteretic nonlinearities in rolling moment due to sideslip. The results presented demonstrate that the nonlinear ML estimation procedure provides a valuable tool which can be conveniently used to validate the mathematical models currently being postulated for aerodynamic phenomena likely to arise in modern high-performance aircraft.

4. Conclusion

In conclusion, the two contributions of this thesis can be broadly summarized as follows. First, a computationally attractive and easy-to-implement maximum likelihood estimation procedure which can handle different nonlinear model structures in a general way has been developed. From the viewpoint of engineering applications, this results in significantly further expanding the scope of estimation techniques as applied to nonlinear dynamical systems. Second, the four applications from flight mechanics reported in this thesis demonstrate that the nonlinear estimation procedure can be efficiently used to generate and validate significantly improved aircraft mathematical models. It is expected that this powerful and flexible tool will pave further way in the analysis of problems in flight mechanics much more conveniently than has been possible to date.

Table I

Non-dimensional derivatives estimated directly using nonlinear model

Flap (deg)	0.54	0.54	2.64	2.64	4.75	4.75	7.22	7.22	9.03	9.03	11 34	11.34
C_{x_0}	−0.0336	−0.0223	−0.0111	−0.0033	0.0059	0.0094	0 0015	0.0173	0.0145	0.0080	0.0176	0.0147
	4.5*	6.9	10.9	32.1	67.1	20.5	95.2	7.4	11.5	12.1	6.7	6.1
C_{x_u}	0.7113	0.7405	0.7313	0.6693	0 6411	0.6920	0.6351	0.6200	0.5945	0.5712	0.5345	0 5993
	0.8	1.0	0.6	0.6	1.3	12.9	0.7	0.9	1 0	0.8	0.9	0.7
C_{x_0}	−0.0744	−0.0902	−0 1049	−0.1014	−0.1108	−0.1166	−0.1042	−0.1159	−0.1126	−0 1017	−0.1105	−0 1106
	2.0	2 0	1.1	1.2	3.6	1.6	1 3	1.1	1.5	1 0	1.1	0 8
C_{z_W}	0.4844	0.4590	0.4935	0.4068	0.4623	0.3533	0.4142	0.3939	0.2903	0.3677	0.3831	0.3456
	1.5	1.7	1.3	1.4	4.0	2.7	2.0	1.8	3.4	1.7	1.9	1.7
C_{z_u}	−4.4262	−4.8759	−4.4890	−4.5900	−4.5326	−4.4517	−4.5539	−4 7404	−4.6017	−4.6563	−4.6093	−4.7913
	0.7	0.7	0.5	0.5	1.0	0.8	0.6	0.6	0.7	0.6	0.6	0 5
C_{z_0}	−0.4993	−0.4129	−0.5356	−0.4318	−0.5119	−0.4106	−0.4926	−0.4493	−0.3746	−0.4501	−0.5055	−0 4462
	1.4	2.0	1.1	1.4	3.6	2.1	1 6	1.5	2.6	1 5	1.5	1.3
C_{m_W}	0.1100	0.1002	0.1085	0.0952	0.0936	0.0834	0.0745	0.0751	0.0564	0.0649	0.0696	0 0562
	1.7	2.0	1 4	1.7	5.2	2.8	2.5	2.1	4.1	2.5	2.7	2.6
C_{m_W}	−1.0857	−1.0917	−1 0864	−1 0671	−1.0941	−1.0987	−1.0426	−1.0472	−1.0620	−1.0777	−1 0749	−1.0856
	0.5	0.6	0.4	0.4	0.8	0.7	0.5	0.5	0.6	0 5	0.5	0.4
C_{m_q}	−25.973	−26.496	−31.253	−30.767	−25.825	−29.017	−29.327	−28.852	−28.698	−30 968	−31 572	−29.046
	1.7	1.6	1.0	1.1	2.5	2.1	1 3	1.5	1.9	1.4	1.4	1.3
C_{m_0}	0 0251	0.0353	0.0296	0.0368	0.0454	0.0535	0.0568	0 0548	0.0755	0.0677	0.0601	0 0727
	7.8	6.3	5.3	4.7	11.0	4.5	3.4	3.0	3.2	2.5	3.3	2 1
$C_{m\dot{w}_0}$	−1.5424	−1.6210	−1.6786	−1.5949	−1.5871	−1.6659	−1 6358	−1.6008	−1.5722	−1.6668	−1.6800	−1.6108
	0.7	0.7	0.5	0.5	1.0	0.9	0.6	0.6	0.8	0.6	0.6	0.6

*%Standard deviation

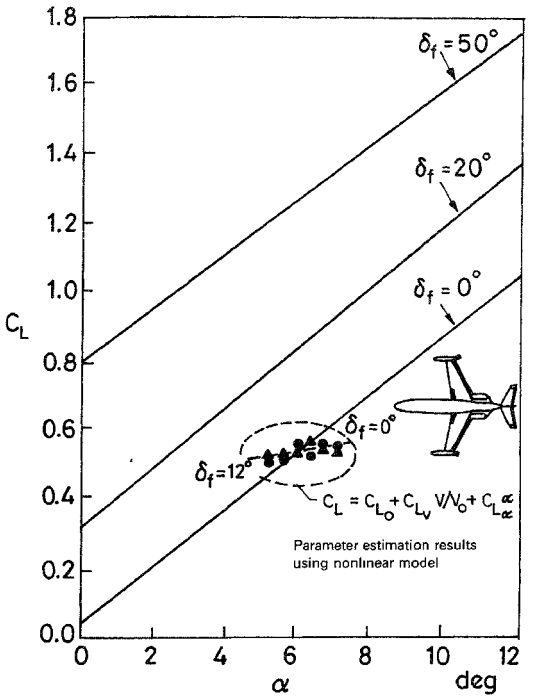

FIG. 1. Lift coefficient as a function of angle of attack and flap deflection.

References

1. JATEGAONKAR, R. V. AND PLAETSCHKE, E. *Nonlinear parameter estimation from flight test data using minimum search methods*, DFVLR, 1983, FB, 83–15.

2. JATEGAONKAR, R. V. Parametric identification of discontinuous nonlinearities, *VII IFAC Symposium on Identification and System Parameter Estimation*, York, UK, 1985, pp. 167–172.

Thesis Abstract (Ph.D.)

Three-dimensional stress analysis of finite thick plates with through cracks by M. N. Bapu Rao.
Research supervisors: K. T. Sundara Raja Iyengar and M. V. V. Murthy (NAL).
Department: Civil Engineering.

1. Introduction

Crack problems of plates with finite thickness and through-the-thickness cracks are frequently encountered in the design of various engineering structures. It is well known that the state of stress in the neighbourhood of the crack front in a plate of finite thickness is invariably three dimensional in nature. It is, therefore, essential that a three-dimensional stress analysis is carried out in order to understand the true behaviour of the stress and displacement fields prevailing in the vicinity of the crack front. Recent three-dimensional investigations[1-3] in this area have raised some pertinent questions concerning the stress and deformation fields existing around the crack front, such as the type of stress singularity all through the plate thickness, nature of the variation of the stress intensity factor (SIF) across the plate thickness and the character of the displacement field along the crack front. Since the questions raised are basic in nature, they can be examined only through a rigorous three-dimensional analysis.

A study of the literature reveals that only a few investigations are available in this area in view of the fact that the mathematical formulation involved is extremely complex and tedious in nature. In particular, even the existing investigations[1,2] on problems dealing with through-crack geometry indicate that they are only qualitative in nature, and no numerical results are available for the physical quantities of interest, such as the SIF. Therefore, it is clear that much work still remains to be done in the area of three-dimensional stress analysis of finite thick plates with through-the-thickness cracks.

In this thesis, a three-dimensional formulation is presented for carrying out the elastic stress analysis of finite thick rectangular plates with through-the-thickness cracks. The stress problem of finite thick plates with through-the-thickness cracks under extensional and bending loadings with mode-I type of deformation are considered for investigation.

2. Solution

The analyses of the extensional and bending problems, which are associated with symmetric and antisymmetric deformations with respect to plate middle plane respectively are carried out separately in a cylindrical coordinate system (r, θ, Z) (fig. 1). The general solution for the extensional problem is formed by considering a linear combination of three independent solutions to governing equations. The general solution for the bending problem is constructed in a similar manner. The general solution for each loading case satisfies the boundary conditions at the stress-free crack and plate surfaces exactly. The boundary conditions at the exterior edges of the plate, which include those associated with the applied extensional and bending loadings, are satisfied in the least square sense. The general solution for each case is then specialized to the region lying in the neighbourhood of the crack front in order to arrive at singular stresses.

3. Results

In the neighbourhood of the crack front where the radial distance is much less than ($r \ll a$) the crack

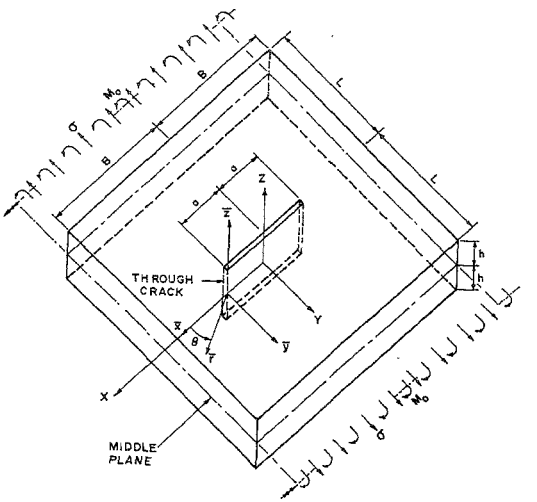

M_0. APPLIED MOMENT; σ: APPLIED TENSION

FIG. 1. A finite thick plate with a through-crack under extensional and bending fields.

length, it is found that the inplane and the transverse normal stresses are singular with an inverse square root singularity ($r^{-1/2}$), while the transverse shear stresses are of the order of unity. The angular variation of the singular stresses is the same as that of plane strain. The SIF is a function of the coordinate in the thickness direction.

In the extensional problem, the SIF is a symmetric function of the coordinate in the thickness direction. It is found to be dependent on the thickness and Poisson's ratios. When the thickness ratio tends to infinity, the SIF reduces to that for the plane-strain porblem. One of the interesting features of the solution is observed in the variation of singular stresses across the thickness, which is found to have a composite character. While it exhibits the character of plane strain in the interior of the plate thickness and that of plane stress (not the generalized plane stress) near the plate faces, it is only in the region lying in between the former two regions that the singular stresses display a true three-dimensional character.

In the case of bending problem also the SIF is a function of both the thickness and Poisson's ratios. The expression for the SIF, which is an antisymmetric function of the coordinate in the thickness direction, reduces to that for the two-dimensional Reissner's bending theory when appropriate mathematical manipulations are carried out.

Parametric studies have been carried out to determine the effect of various geometric parameters, in particular the thickness and Poisson's ratios on the character of SIF. For particular cases the results

are in reasonably good agreement with those of finite element, boundary integral equations and photoelastic methods[4-6].

4. Conclusions

The nature of singular stresses in the neighbourhood of the crack front indicates that the only type of singularity achieved is that of the inverse square root all through the plate thickness. The SIF is a function of the thickness and Poisson's ratios. The displacement components along the crack front are finite.

References

1. SIH, G. C., WILLIAMS, M. L. AND SWEDLOW, J. L. — *Three dimensional stress distribution near a sharp crack in a plate of finite thickness*, 1966, AFML-TR-66-242.
2. HARTRANFT, R. J. AND SIH, G. C. — The use of eigenfunction expansions in the general solution of the three-dimensional crack problems, *J. Math. Mech.*, 1969, **19**, 123–138.
3. FOLIAS, E. S. — Method of solution of a class of three-dimensional elastostatic problems under Mode-I loading, *Int J. Fracture*, 1980, **16**, 335–348.
4. RAJU, I. S. AND NEWMAN, J. C. JR. — *Three-dimensional finite element analysis of finite thickness fracture specimens*, NASA-TND-8414.
5. ALWAR, R. S. AND RAMACHANDRAN NAMBISSAN, K. N. — Three-dimensional finite element analysis of cracked thick plates in bending, *Int. J. Numer Meth. Engng*, 1983, **19**, 293–303.
6. VILLARREAL, G., SIH, G. C. AND HARTRANFT, R. J. — Photoelastic investigation of a thick plate with a transverse crack, *J. Appl. Mech., ASME*, 1975, **42**, 9–14.

Thesis Abstract (Ph.D.)

Studies on thermally grown titanium oxide overlayers on titanium for electronic components
by R. Padma.
Research supervisors: M. Satyam and K. J. Rao.
Department: Electrical Communication Engineering.

1. Introduction

This thesis deals with the study of the physical structure of thermally grown titanium oxide overlayers on titanium and their electrical characteristics, with a view to use them as thermistors and varistors.

2. Experimental and discussion

Titanium oxide has been grown on clean titanium plates by heating them in air and steam over a temperature range of 700 to 1000°C for varying time durations *i.e.* from $\frac{1}{2}$ to 5 h^1. These overlayers have been heated in vacuum to impart *n*-type semiconductivity. Later they have been stabilised from the point of resistance values.

The V-I characteristics of these samples have been measured at different temperatures[2] (fig. 1). It has been found that the characteristic changes with temperature. Further at low voltages, it has been

observed to be nonlinear, whereas at higher voltages, it is linear. The extent of nonlinearity leads to the use of the overlayers as varistors with the varistor index having values ranging between 1.0 and 2.5. The origin of nonlinearity has been examined and it has been concluded through analysis that the nonlinearity arises due to thermionic emission process at the grain boundaries. The equation governing this process has been given by

$$I = aAT^2 \exp\left[-\frac{(V_B - ev_g)}{kT}\right]$$

where I is the total current through the oxide film, A the constant of thermionic emission, a the area of cross section of current flow, V_B the barrier potential at the grain boundary and V_g the voltage across the grain boundary.

The temperature dependence of the resistance at any particular voltage has been explained based on the behaviour of semiconductors and the grain boundaries with temperature. The resistance has been found to vary with temperature according to the relation

$$R = R_0 \exp\left[B\left(\frac{1}{T} - \frac{1}{T_0}\right)\right]$$

where B is called the thermistor constant. B has been found to lie in the range 100 to 400°K.

Considerable amount of effort has been put in to arrive at a proper technique of stabilisation[3]. The structure of the oxide overlayer has been looked at experimentally as well as theoretically. Several X-ray diffractograms have been taken and through them it has been concluded that oxides prepared at low temperatures or for short durations have several oxide phases The instability has been attributed to the gradual transformation of these oxides to the stable rutile phase with time. To understand the way in which the various phases of oxides arise, a theoretical model for the growth of titanium oxide based on diffusion and chemical absorption of oxygen passing through the film has been proposed. Differential equations describing the transformation of titanium into titanium oxide under the above conditions have been arrived at and solutions of these equations with appropriate boundary conditions have been obtained with the help of DEC10 computer. The differential equation formulated for the purpose of the estimation of the oxide structure in the overlayer is

$$\frac{dN(x,t)}{dt} = D\frac{d^2N(x,t)}{dx^2} - C.N(x,t).\xi(x,t)$$

where N is the number density of free oxygen atoms, D the diffusion constant, C the proportionality constant, $\xi = (2 - I)$ where I is the stoichiometric index in the titanium oxide TiO_I and I can take values from 0 to 2.

It has been calculated using the equation

$$\frac{dI}{dt} = \frac{C.N.\xi}{n_0}$$

where n_0 is the number of titanium atoms per unit volume.

The solutions indicate that the stoichiometric composition (I) of oxygen varies from zero at the metal-oxide interface to that of titanium dioxide at the top of the surface. A typical variation of I with depth from surface for different time durations is shown in fig. 2. At any particular point in the oxide, the oxygen content and the thickness of the oxide are found to increase with time. It is thought that titanium oxide can exist only in certain stable forms and a method of finding out the percentages of these various stable oxides at different points of the oxide has been developed. From the model

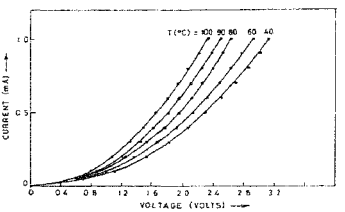

FIG. 1. Measured voltage-current characteristics of titanium oxide sample at different temperatures.

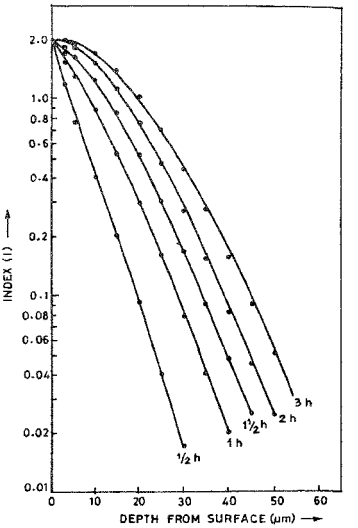

FIG. 2. Computed variation of index along the depth for different time durations.

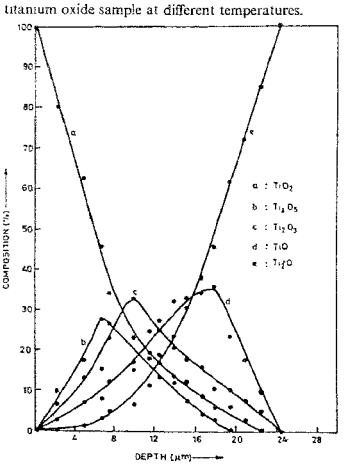

FIG. 3. Variation of composition (%) of different oxides along the depth.

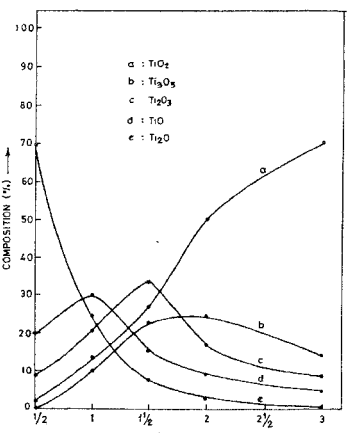

FIG. 4. Variation of composition (%) of different oxides with time.

proposed, it is concluded that these stable oxides combine in appropriate proportion to give that particular TiO_I, at each layer. Figures 3 and 4 show typical variations of percentage of oxide with depth and time, respectively. From fig. 3, it can be observed that TiO_2 (with $I = 2$) has the highest percentage at the surface and decreases towards the metal-oxide interface while Ti_2O (with $I = 0.5$) shows a reverse lined and the remaining oxides show a maximum in the middle of the oxide layer. This shows that the oxides with higher oxygen content are near the top of the surface and with lower oxygen content are near the oxide-metal interface. From this type of variation, the oxide is considered to be a layered structure. From fig. 4, it can be seen that the oxide starts growing at different depths at different instances. Through this analysis, the instability in the resistance values of the oxides has been attributed to the gradual transformation of lower oxides to higher titanium oxide at the top layers of the oxide.

References

1. STRINGER, J. *Acta Metall.*, 1960, **8**, 758–766.
2. EARLE, D. M. *Phys. Rev.* (2), 1942, **61**, 56–62.
3. JARDIN, C. *et al* *Titanium '80 Science and Technology*, Vol. 4, p. 2819.

Thesis Abstract (Ph.D.)

Studies on the realization of magnetoresistors based on composite materials by T. Arivoli.
Research supervisors: M. Satyam and K. Ramkumar.
Department: Electrical Communication Engineering.

1. Introduction

Conventional magnetoresistors, *i.e.*, resistors whose values of resistance change with an applied magnetic field, are usually prepared from semiconductors such as indium antimonide. In these devices, the magnetoresistance effect is enhanced by shorting the Hall voltage generated across the semiconductor due to an applied magnetic field. This is achieved either by making the sample with an annular ring shape (carbino disc)[1] or by incorporating shorting links in the material (InSb-NiSb eutectic)[2]. The zero-field resistance of the carbino disc magnetoresistor is very small ($\sim 1\Omega$), and hence, cannot be used directly in electronic circuits. Further, both the types of magnetoresistors (disc and eutectic) need special fabrication techniques like unidirectional solidification of eutectics or realization of semiconductor films or crystals with specific geometry. Thus, there is a need to develop magnetoresistors which can be realized with simpler technology, but have a performance comparable to the conventional magnetoresistors.

It has been predicted[3] that the magnetoresistance effect can be realized by proper coupling of interactions in a multiphase composite material. When magnetic particles are dispersed in an elastic material, a magnetoelastic composite results. If a magnetic field is applied to this composite, a deformation (or strain) is produced in the composite due to the interaction between the magnetic particles. If this deformation is transferred to a thin composite elastic resistive sheet, it leads to a change in the resistance of the sheet. An attempt has been made to conceive and develop magnetoresistors based on the above-mentioned interaction in composites.

2. Experimental and discussion

The magnetoresistor developed by us (fig. 1) consists of an elastic magnetic cylinder in which a thin resistive sheet is sandwiched in the centre. The magnetic cylinder is made of a composite of rubber and iron powder. The resistive sheet is made of a composite of rubber and metal powder (brass). The change in resistance (in this device), as a function of magnetic field, has been measured. A typical variation is shown in fig. 2. It may be seen from this figure that the change in resistance is small at low fields. At higher fields, it increases steeply with magnetic field and finally tends to saturate. Typical values of the relative change of resistance ($\Delta R/R_0$) for this type of magnetoresistor are given in Table I along with the corresponding values for other types of conventional magnetoresistors. From this table it may be seen that the magnetoresistor based on a composite gives rise to a change of resistance comparable to that of conventional magnetoresistors.

It is well-known that the zero-field resistance at a composite magnetoresistor can be varied over a wide range by changing the composition of rubber and conducting particles in the resistive sheet. It has been found that the change in resistance in this type of magnetoresistor depends on parameters like its shape and the composition of the materials of the magnetic cylinder. Detailed theoretical calculations of the magnetoresistance and its dependence on the factors mentioned above have been carried out based on a model proposed for the composite.

Thus, the work reported in this thesis clearly indicates the possibility of realizing magnetoresistors based on composites which require relatively simpler technology, but provide a performance comparable to that of conventional magnetoresistors.

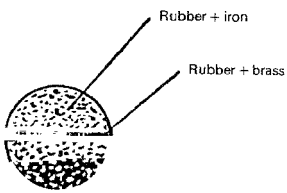

FIG. 1. Cross-section of the sample.

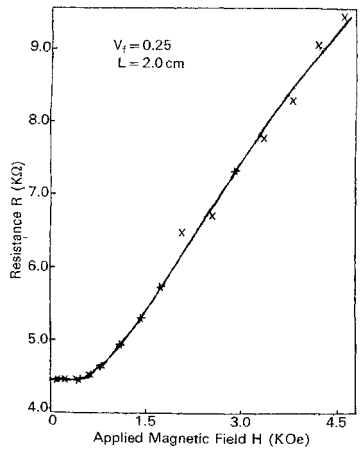

FIG. 2. Measured variation of resistance with applied magnetic field for a typical sample. Volume fraction of iron (v_f) = 0.25; Length of the sample (L) = 2.0 cm; Diameter of the sample (d) = 1.0 cm.

Table I
Typical values of the relative change of resistance ($\Delta R/R_0$) of various magnetoresistors

Type	$\Delta R/R_0$ at 8 KOe
Carbino disc[1]	15
InSb-NiSb eutectic[2]	
aligned	12
unaligned	2
Cd_3As_3-NiAs eutectic[4]	0.4
Present composite	1(at 4.5 KOe)

References

1. WEISS, H. — *Structure and application of galvanomagnetic devices*, 1969, Pergamon.
2. WEISS, H AND WILHELM, M — *Z. Physik*, 1963, **176**, 399–408.
3. VAN SUCHTELEN, J. — *Philips Res. Rep.*, 1972, **27**, 28–37.
4. ELLIOTT, C. T. AND HISCOCKS, S. E. R. — *J. Phys. D (Appl. Phys.)*, 1969, **2**, 1083–1087.

Thesis Abstract (Ph.D.)

Thermal and chemical stabilities of three Fe-Ni-base metallic glasses by V. S. Raja.
Research supervisors: S. Ranganathan and Kishore.
Department: Metallurgy.

1. Introduction

Iron and iron-nickel-base metallic glasses possess an attractive combination of mechanical[1], magnetic[2] and chemical properties[3]. However, a serious lacuna which restricts their application is the poor thermal stability owing to their metastable character. Devitrification is found to affect the attractive physical, chemical and mechanical properties, while a few of the properties like magnetism and superconductivity are improved on partial crystallization[4]. This necessitates a systematic study on the thermal stability and associated properties of these materials. It is the aim of the present investigation to understand the influence of Mo and Si on thermal and chemical stabilities of Fe-Ni-B glasses.

2. Experimental techniques

Three commercial glasses of compositions $Fe_{40}Ni_{40}B_{20}$ (Vitrovac 0040), $Fe_{40}Ni_{38}Mo_4B_{18}$ (Metglas 2826 MB) and $Fe_{36}Ni_{39}Mo_4Si_6B_{12}$ (Vitrovac 4040) have been chosen to study the influence of Mo and Si. The thermal stability has been followed using differential scanning calorimetry (DSC), X-ray diffraction (XRD) and optical and electron microscopy techniques, while potentiodynamic polarisation, ESCA and microscopy techniques have been employed to understand the chemical stability of these alloys.

3. Crystallization

The glass Vitrovac 0040 has been found to crystallize into four types of crystals simultaneously, *viz.*, (A) γ-FeNi + orthorhombic $(FeNi)_3B$, (B) γ-FeNi + Fcc $(FeNi)_{23}B_6$, (C) γ-FeNi solid solution and (D) an unknown Fe-rich phase. The first three of them are shown in fig. 1.

The overall transformation kinetics of the A-type crystals having the highest growth rate shows an Avrami exponent of 2.08—an unusually small value for an eutectic crystallization—which has been ascribed to both the athermal nucleation and anisotropic growth behaviour. The present study yields the activation energies of 237 kJ mol^{-1} for crystallization and 290 kJ mol^{-1} for growth. The microstructural observation reveals that these crystals grow in a rod-like morphology with an aspect ratio ~ 4 in the fully crystallized condition and twinning of the orthorhombic phase. The interlamellar spacings in these crystals have been found to decrease with increase of temperature. The diffusion coefficients determined from the interlamellar spacings range from 4.77×10^{-18} to 1.95×10^{-17} m^2 s^{-1} for the temperatures between 643 and 673 K.

The B-type eutectic crystals obey a linear rate law with an activation energy of 360 kJ mol^{-1} for the growth process. In contrast to A-type crystals, B-type crystals are found to have a cuboidal morphology. Furthermore, it is also observed that the C- and D-type crystals grow with spherical morphologies.

It has been proposed that Vitrovac 0040 separates into two glasses, G_1 and G_2, before crystallization takes place. The former glassy phase leads to A-type eutectic crystals, while G_2 can transform into primary crystals of γ-FeNi and G_3. The latter subsequently crystallizes into B-type crystals by the eutectic mode.

The addition of Mo, as revealed by $Fe_{40}Ni_{38}Mo_4B_{18}$, results in two-stage crystallization. The primary crystallization of γ-FeNiMo is followed by the polymorphic crystallization of fcc$(FeNi)_{23}B_6$

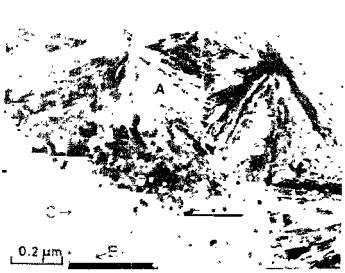

FIG. 1. Transmission electron micrograph of partially crystallized Vitrovac 0040.

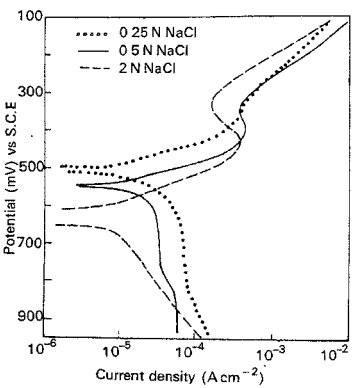

FIG. 2. Typical polarisation curves of Vitrovac 0040 in NaCl medium showing the increase in corrosion rate with concentration of NaCl.

crystals. The pseudo grain structure which appeared in TEM image and the broad XRD peak have been attributed to incipient phase separation of the glass during melt quenching itself. However, evidence for phase separation is not strong.

The high-activation energies for the crystallization of γ-FeNiMo and fcc$(FeNi)_{23}B_6$, respectively 270 and 375 kJ mol^{-1}, as determined from Kissinger plots and 285 and 365 kJ mol^{-1} from Ozawa plots imply that Mo imparts stability against crystallization. Further, it found that Mo aids the formation of fcc$(FeNi)_{23}B_6$ phase in preference to O-$(FeNi)_3B$ phase. It is noted that while γ-FeNiMo crystallites have almost spherical morphology, the fcc$(FeNi)_{23}B_6$ crystallites reveal a faceted morphology.

Further substitution of B with Si$(Fe_{39}Ni_{39}Mo_4Si_6B_{12})$ leads to a dramatic change in the phase relationship. Thus $Fe_{39}Ni_{39}Mo_4Si_6B_{12}$ crystallizes sequentially into α-Fe, hexagonal Ni_5Si_2 and γ-FeNiMo. These reactions have been classified as primary and secondary crystallizations, and polymorphic reaction, respectively[5].

The activation energies for the crystallization of the glass into α-Fe, hexagonal Ni_5Si_2 and γ-FeNiMo, respectively, have been found to be 490, 550 and 449 kJ mol^{-1} from Kissinger method and 480, 600 and 440 kJ mol^{-1} from Ozawa method. This indicates that Si enhances the stability of the glass further.

The α-Fe phase formed at the beginning of devitrification is found to be metastable and transforms to γ phase, whose lattice parameter is close to that of γ-FeNiMo phase formed from the glass. The characteristics of this transformation is that α-Fe transforms faster on the dull side than on the bright side. The transformed γ phase shows preferential orientation along (111). At temperatures above 1023 K, a new phase, namely, bct $(Fe_{1-x}Ni_x)_3B$ forms from the already crystallized glass whose volume fraction is found to be small. While α-Fe, hexagonal Ni_5Si_2 and γ-FeNiMo are found to have spherical morphology, the bct $(Fe_{1-x}Ni_x)_3B$ has a needlelike morphology containing twins in it.

4. Corrosion

The electrochemical corrosion behaviour of the three glasses has been investigated in both chloride and sulphate media.

The potentiodynamic polarisation study of $Fe_{40}Ni_{40}B_{20}$ shows that the corrosion rate increases with chloride ion concentration. On the other hand, the tendency for passivation gets enhanced with increase in chloride ion concentration. Both polarisation and ESCA studies reveal that the glass undergoes selective dissolution in hydrochloric acid depending on the potential the glass is being held. The sequence of dissolution in the order B, Fe and Ni as B^{3+}, Fe^{3+} and Ni^{2+} [respectively at E_R, −120 and 0 mV (SCE)] is in accordance with the well-known Wagner's mixed potential theory of galvanic corrosion. It is noted that the glass does not passivate even in neutral sulphate medium.

The Mo containing glass $Fe_{40}Ni_{38}Mo_4B_{18}$ passivates in neutral and slightly acidic sulphate solutions, while failing to passivate in H_2SO_4 solutions. However, replacement of B with Si results in passivation of the glass $Fe_{39}Ni_{39}Mo_4Si_6B_{12}$ in H_2SO_4 solutions also. Further, it is found that the addition of 6 at%Si reduces the critical current density by about one order of magnitude and the passivation current density to a smaller extent. However, both the glasses are susceptible to pitting and crevice corrosion although they contain Mo and Si as revealed by the high critical current density. It is observed that both the glasses do not passivate in chloride medium.

An analysis of the passive film by means of ESCA indicates that the passive film consists of oxides of Fe, Ni and Mo and is free from B and Si. While Fe and Ni are in + 3 and + 2 states, respectively, Mo

has been found to exist in + 6 state on the surface and + 4 state in the bulk of the passive film. Hence it is proposed that though Mo can aid the repassivation of the pits, the oxides of Fe and Ni which constitute the passive film offer poor resistance against local reduction of the passive film during pitting, in the absence of good passivating elements like Cr and P.

The addition of Mo does not seem to affect the corrosion resistance significantly in either HCl or H_2SO_4 solutions. On the other hand, Si has a deleterious effect in H_2SO_4, while imparting no significant change in HCl solution.

5. Effect of devitrification on corrosion

The effect of crystallization on chemical stability has been followed. It is found that devitrification of $Fe_{40}Ni_{40}B_{20}$ does not lead to significant deterioration of corrosion resistance in 1N NaCl. While the thermal relaxation of the glass improves the corrosion resistance slightly, corrosion rate has been found to increase in the partially and fully crystallized condition[5-7].

While the initial formation of γ-FeNiMo in $Fe_{40}Ni_{38}Mo_4B_{18}$ glass does not influence the corrosion rate in the partially crystallized condition in 0.5N H_2SO_4, a seven-fold increase is observed in the fully crystallized glass where fcc$(FeNi)_{23}B_6$ coexists with γ-FeNiMo. However, the corrosion resistance decreases on further annealing due to grain coarsening.

The corrosion rate of $Fe_{39}Ni_{39}Mo_4Si_6B_{12}$ is greatly influenced by the preferential dissolution of α-Fe. In its presence the corrosion current is enhanced as high as 33 times, which, however, reduces to a value closer to that of amorphous alloy when α-Fe fully transforms.

References

1. DAVIS, L. A., RAY, R., CHOU, C.-P. AND O'HANDLEY, R. C. — *Scr. Metall.*, 1976, **10**, 541–546.
2. DUWEZ, P. AND LIN, S. C. H. — *J. Appl. Phys.*, 1967, **38**, 4096–4097.
3. NAKA, M., HASHIMOTO, K. AND MASUMOTO, T — *J. Japan Inst Met.*, 1974, **38**, 835–842.
4. LUBORSKY, F. E. — *Mater. Sci. Engng*, 1977, **28**, 138–144.
5. RAJA, V. S., KISHORE AND RANGANATHAN, S. — *Key Engng Mater.*, 1987, **13–15**, 311–314.
6. RAJA, V. S., KISHORE AND RANGANATHAN, S. — *Rapidly quenched metals-V*, Vol. II, (Steeb, S. and Warlimont, H. V., eds), 1985, pp. 1485–1488, North-Holland.
7. RAJA, V. S., KISHORE AND RANGANATHAN, S. — *Corrosion*, 1988, **44**, 263–268.

Thesis Abstract (Ph.D.)

Magnetohydrodynamic flow and diffusion in channels or pipes with some physiological applications by K. S. Deshikachar.
Research supervisor: A. Ramachandra Rao.
Department: Applied Mathematics.

1. Introduction

The thesis deals with the study of effects of magnetic field on the flow and diffusion in channels or pipes of uniform or non-uniform cross-section in the presence of an applied magnetic field. The thesis is divided into seven chapters, each dealing with a specific type of problem. The first four chapters deal with the flow and the last three with diffusion problems.

2. Results and discussion

In the first chapter, the steady flow and oxygenation of a homogeneous, incompressible, viscous, conducting fluid in a channel of slowly varying cross-section is investigated in the presence of a uniform transverse magnetic field. The governing equations are perturbed using a parameter $\delta(\ll 1)$ which is the ratio of the half-mean width of the channel to the characteristic length along the channel over which significant changes in the flow quantities occur. An analytical solution is obtained for the equations governing the flow. This solution is then used to obtain the effects of magnetic field on the oxygenation in a membrane oxygenator in the form of a wavy channel. As the equations of partial pressure remain nonlinear even after perturbation, a numerical solution is presented using Crank-Nicholson implicit method. The effect of various parameters on the flow field, oxygen concentration and possible occurrence of separation and reattachment are discussed for symmetric or asymmetric channels, of physiological interest. The convergence of the perturbation series is also discussed. It is observed that the separation in the flow occurs at a high Reynolds number in this case compared to the hydrodynamic[1] case which is favourable physiologically and the application of a magnetic field has some effect on local oxygen concentration but has a little effect on saturation length.

The oscillatory flow of a homogeneous viscous conducting fluid in a channel of non-uniform cross-section is studied in Chapter II. Using the same perturbation parameter $\delta(\ll 1)$, as in the previous chapter, the first, second harmonics and the steady-streaming solutions are obtained for a flow in which the volume flux is prescribed. The parameters that govern the flow are α, the Womersley number, H, the Hartmann number and Re, the Reynolds number. The possibility of separation in the flow is discussed for channels with sinusoidal walls. The oscillatory flows, over surfaces which are not straight, exhibit a steady-streaming component due to nonlinearity of the governing equations of motion. The steady-streaming velocity is discussed for channels with sinusoidal symmetric, asymmetric or tapered walls[2]. The solutions for large α are also obtained using the method of matched asymptotic expansions. It is interesting to observe that there is no difficulty in matching the solutions here in comparison with the non-magnetic case[3] as the magnetic field provides another appropriate length scale necessary for matching.

Chapter III deals with the oscillatory flow in a circular tube of varying cross-section in the presence of a uniform magnetic field applied along the axis of the tube. An analytical solution of the perturbation problem is obtained for a small parameter characterising the slope of the wall and for different Reynolds, Womersley and Hartmann numbers. The induced field is also taken into account in this chapter unlike in the first two chapters. The steady-streaming phenomena, the pressure and

shear stress distributions on the wall of a constricted or dilated tube for various parameters governing the flow are discussed.

A physiological-type flow in a straight circular tube in the presence of a uniform transverse magnetic field is considered in Chapter IV. The pressure gradient is mathematically modelled by a Fourier series of which the second partial sum resembles very closely the observed form of the pressure gradient in a living body. The governing equations are solved exactly by using the method of Laplace transforms. It is found that the effect of a magnetic field is to reduce the magnitude of velocity near the centre region of the pipe. The coefficients of amplitude and phase lag of the mean velocity are also reduced in the presence of a magnetic field.

The effect of flow oscillations on the molecular diffusion of a solute in a channel is investigated in the presence of a transverse magnetic field in Chapter V. The approximate solutions are presented up to second order for small Womersley number which is used as a perturbation parameter. The effect of flow oscillations on concentration distribution is discussed for a specific type of initial concentration distribution for different values of Womersley and Hartmann numbers. The diffusion enhancement due to the flow is explained in terms of an equivalent diffusion coefficient.

Chapter VI deals with the dispersion of a solute in an oscillatory flow between two parallel porous plates in the presence of a uniform transverse magnetic field. Exact solutions for the equations governing the flow and diffusion are obtained. The coefficient $H = (\mathrm{Rh}^4/V_1^2)$, is evaluated numerically, when R is the increase in flux, 2h the width of the channel and V_1 the tidal volume. It is found that the value of H decreases with an increase in Hartmann number M or suction parameter R_1 whereas it increases with an increase in Womersley number W_0 or Schmidt number σ_0.

An exact solution[4] to the unsteady convective diffusion equation for the dispersion of a solute in a fully developed laminar flow in an annular pipe is presented in the last chapter. The dispersion coefficients[5] are evaluated as a function of time using a generalised dispersion model which is valid for all time. It is observed that the axial dispersion of mean concentration decreases with an increase in the radius of the inner cylinder.

References

1. CHOW, J. C. F. AND SODA, K. — Laminar flow and blood oxygenation in channels, with boundary irregularities, *Trans. ASME, J. Appl. Mech.*, 1973, **40**, 843–850.

2. SMITH, F. T. — The separating flow through severely constricted symmetric tube, *J. Fluid Mech.*, 1979, **90**, 725–754.

3. GROTEBERG, J. B. — Volume cycled oscillatory flow in a tapered channel, *J. Fluid Mech.*, 1984, **141**, 249–264.

4. GILL, W. N. AND SANKARASUBRAMANIAN, R. — Exact analysis of unsteady convective diffusion, *Proc. R. Soc. A*, 1970, **316**, 341–350.

5. TAYLOR, G. I. — Dispersion of soluble matter in solvent flowing slowly through a tube, *Proc. R. Soc. A*, 1953, **219**, 186–203.

Thesis Abstract (M.Sc.(Engng))

Photoelastic determination of stress intensity factors—New approaches and application to T-root of steam turbine blade by M. Mohan Prabhu.
Research supervisors: L. S. Srinath and S. K. Bhave (BHEL).
Department: Mechanical Engineering.

1. Introduction

The concept of stress intensity factors (SIF) is a major breakthrough in the the field of fracture mechanics. The application of photoelasticity for the experimental evaluation of SIFs is very popular because of the advantages this method has over the others like its simplicity and versatility in addition to the pictorial depiction of the phenomenon. But a major limitation of this application was the need to make measurements in an extremely small zone close to the crack tip. In the course of the present work methods were developed which use photoelastic data taken in a convenient zone not too close to the crack tip to evaluate both pure mode I and mixed-mode SIFs K_I and K_{II}.

In the photoelastic models cracks are simulated using artificial notches. The dimensions of these notches to correctly simulate the crack behaviour were varied depending upon the investigator. The reported notch geometries were also quite difficult to make using the normally available facilities in any research laboratory. In the present work this problem was also tackled to arrive at a simple notch geometry to simulate the crack.

The analysis of mixed-mode problems involves solution of non-linear equations. This poses a problem in many cases where one cannot have an idea of the order of the SIFs *apriori*. If one of the SIFs could be obtained independently this problem gets solved. A new concept of equivalent mode I SEN (single edge notch) specimen for the solution of mixed-mode problems was also developed in the course of the present work which tackles the above problem.

2. Experimental

The modified method developed for the pure mode I case involves fringe-order measurements along various radial lines in a convenient zone of $r/a = 0.2$ to 1.0, where r is the polar distance of the data point from the crack tip and a the crack length. The values for each radial line are then used to evaluate K_I by gradually increasing the order of the polynomial accounting for the far-field effect till convergence to the desired degree of accuracy is obtained. Average value of K_I is then determined from the values obtained for the various radial lines. Experimental validation of this method on SEN specimen and cracked annular disc has given good results.

The problem of making an artificial crack in a photoelastic model was studied in detail. Starting with trials at making natural cracks under fatigue loading in epoxy models with starter notches, various artificial notches reported to simulate cracks were tried. The practical difficulties of making these with the normally available facilities in any research laboratory led to the work of finding out a simple notch to simulate the crack. It was conclusively proved that a simple notch of approximately 0.5 mm (or less) width which could be easily cut using a normal jig saw could be used to simulate a crack of equal length when employing the modified method for the determination of mode I SIF. The same notch geometry was employed in further work on mixed-mode analysis, etc.

The improved method developed for the mixed-mode case involving K_I and K_{II} requires just four distance measurements in its simplest form. However, to check the consistency, three angles are

chosen around θ_m, the mean vertex angle of the two isochromatic loops of interest which lie in the zone $r/a = 0.2$ to 1.0. Measurements are limited to the forward tilting loops only as the other loops, probably being in the already cracked zone, give erroneous results. The composite SIFs are first computed for each of the three angles and then taking two of these angles at a time the individual values of K_I and K_{II} are computed by iterative procedures. The average values of K_I and K_{II} are determined from those obtained for the different sets of angles. This method has been experimentally validated on SEN specimens with various inclined cracks.

During the course of this work an interesting observation was made. The superposition of different shear stresses over given normal stresses rotates the crack-tip isochromatic fringe loops as a rigid body about the crack tip maintaining the included angle constant for any given constant normal stress. This led to the development of the concept of equivalent mode I SEN specimen for the solution of mixed-mode problems. K_I can be determined in a mixed-mode problem by making measurements on an equivalent pure mode I SEN specimen or from previously obtained calibration curves. Then K_{II} can be determined easily without resorting to the iterative solution of any non-linear equation. This was experimentally validated on SEN specimen.

Lastly, a practical application of the new developments was taken up. Cracking of T-roots of steam-turbine blades was analysed. The most likely location of crack initiation and its direction of initial propagation were first determined by analysing an uncracked blade photoelastically employing the shear difference technique to obtain the individual values of the stresses in the critical zone and employing the relevant theories of failure. Then further crack-growth studies were carried out on T-root models with and without starter notches and also by inspection of prototype blades failed in service. The curved cracks were produced in the photoelastic models by using suitably shaped thin stainless steel foils which were embedded in the model stock during the casting stage itself and subsequently removed after curing. These models were annealed to remove any initial stresses caused by the foils and analysed using the improved method developed for the determination of mixed-mode SIFs. The critical crack length in the prototype T-root was determined employing the K_{IC} criterion as well as the energy release rate criterion in a two-dimensional idealisation of the T-root.

3. Conclusions

The present work has contributed a modified method for the pure mode I problem and an improved method for the mixed-mode problem involving opening and sliding deformations for the photoelastic determination of SIFs, K_I and K_{II}, from measurements done in a convenient zone slightly away from the crack tip, thus overcoming the major limitation of the existing photoelastic methods[1-6] to determine SIFs. It has also been helpful in simplifying the crack simulation using an easily made artificial notch. In addition, an alternative approach to determine K_I directly from the geometrical parameters of the crack-tip isochromatic fringe loops in a mixed-mode case has been developed. Extension of this concept for the determination of K_{II} also has been suggested. In addition to validating the developed methods on geometries with known theoretical solutions, the improved method has been applied to the practical case of a cracked T-root of a steam-turbine blade. Two computer programmes have also been developed to facilitate computational case with the modified and improved methods for the photoelastic determination of SIFs.

References

1. SMITH, D. G. AND SMITH, C. W. Photoelastic determination of mixed-mode SIFs, *Engng Fracture Mech.*, 1972, **4**, 357–366.

2. GDOUTOS, E. E. AND THEOCARIS, P. S — A photoelastic determination of mixed-mode SIFs, *Expl Mech.*, 1978, **18**, 87–96.

3. SANFORD, R. J. AND DALLY, J. W — A general method for determining mixed-mode SIFs from isochromatic fringe patterns, *Engng Fracture Mech.*, 1979, **11**, 621–633.

4. IOAKIMIDIS, N. I. AND THEOCARIS, P. S. — On the photoelastic determination of complex SIFs, *Engng Fracture Mech.*, 1979, **12**, 463–468.

5. COTTRON, M. AND LAGARDE, A. — Far field method for the determination of mixed-mode SIFs from isochromatic fringe patterns, *Solid Mech. Arch.*, 1982, **7**, 1–18.

6. SRINATH, L. S., SRINIVASA MURTHY, N. AND HARESH, T. V. — Determination of SIFs for cracks in tubes under torsion, *Expl Mech.*, 1983, **23**, 262–267.

Thesis Abstract (M.Sc.(Engng))

Some studies on volume change and strength behaviour of soils as affected by environmental factors by T. G. Sitharam.
Research supervisors: K. S. Subba Rao and P. V. Sivapullaiah.
Department: Civil Engineering.

1. Introduction

The soil in nature is continuously under the influence of everchanging climate, which not only contributes to the formation of soils, but also affects the soil properties. Besides, with growing industrialization coupled with waste disposal on land, the nature of porefluid varies considerably; so much so, in the present day context, studies on the behaviour of soils under the influence of climatic and pore-fluid changes assume importance.

The present investigation is an attempt in understanding clay-organic pore-fluid interactions, to check in the first place, whether highly ligative organic molecules result in clay behaviour similar to those produced by weakly ligative molecules. Soil properties like liquid and shrinkage limits, swelling potential and consolidation behaviour have been considered. Secondly, the influence of climate on swelling, shrinkage and strength have been investigated particularly with a view to understand how these properties change as the soil with water as pore fluid undergoes shrinkage.

2. Soils and pore fluids used

Commercially available kaolinite and montmorillonite, natural red earth and black cotton soil were used in this study. Different pore fluids, benzene, dioxane, acetone, methanol, ethanol, dimethyl sulphoxide (DMSO), dimethyl formamide (DMF), and water having a wide range in their bulk properties were used.

3. Results

3.1. *Effect of pore fluid on liquid and shrinkage limits*

It is well recognised that the engineering behaviour of soils is dependent on the interaction of clay

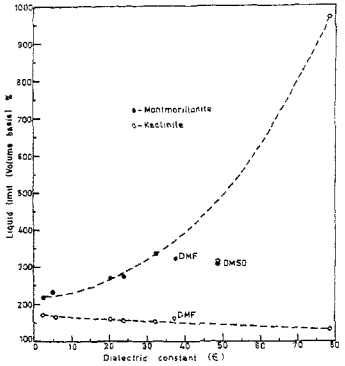

FIG. 1. Relationship between liquid limit and dielectric constant.

particles present in the soils with pore fluids. According to the double-layer theory, these interactions depend on the dielectric constant of the pore fluids. Figure 1 shows the effect of pore fluids on the liquid limit of clays. The striking feature of this figure is the drastic reduction of liquid limit of montmorillonite and the significant increase of the same for kaolinite (from the general trend suggested by dielectric constant) in the presence of highly ligative organic molecules like DMF and DMSO. Exactly opposite trends are observed with the shrinkage limit behaviour. The clay-organic molecule interactions have been explained in this thesis on the basis of fabric changes caused by clay-organic molecule bonding as evidenced by infrared, spectral and X-ray diffraction studies. Figure 2a shows the mechanism of mode of bonding with montmorillonite and 2b shows the particle association of kaolinite in the presence of ligative organic molecules.

3.2. *Volume change behaviour*

A non-dimensional modified free-swell index, ($= V - V_s/V_s$ in which V and V_s stand for sediment volume of soil and volume of soil-solids, respectively), has been proposed to eliminate the inaccuracies in the volume measurement of free swell and differential free-swell tests[2,3]. Modified free-swell tests and swelling-consolidation tests on Procter-compacted samples of clays with different pore fluids are

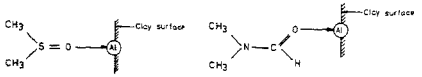

(a) With DMSO molecule. (b) With DMF molecule.

FIG. 2a. Mode of attachment of DMSO and DMF with montmorillonite.

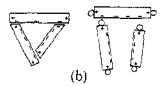

(a) (b)

In the presence of (a) water, and (b) organic molecules.
O-Organic molecule.

FIG. 2b. Particle associations of kaolinite.

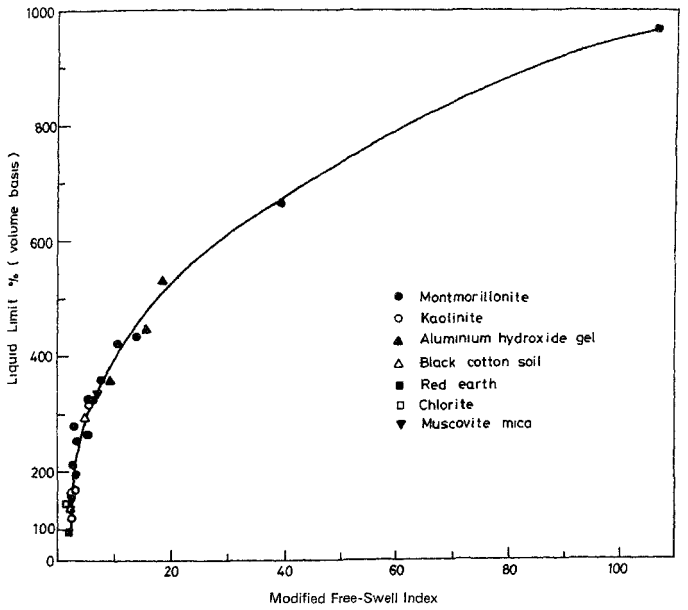

FIG. 3. Relationship between modified free-swell index and liquid limit %(volume basis).

conducted to throw light on the volume-change behaviour of clays in the presence of ligative organic molecules.

The liquid limit and the proposed modified free-swell index have a unique relationship (fig. 3).

3.3. *Shrinkage of soils under varying humidity and temperature*

How the moisture content, degree of saturation, dry density, void ratio and even strength change as the soil shrinks have been closely examined. During shrinkage, changes in volume of air and water and total volume take place depending on whether the shrinkage is structural, normal or residual. Further, the experimental results have revealed a straight line relationship between the void ratio and volumetric shrinkage, based on which shrinkage potential can be predicted given the changes in the void ratio.

3.4. *Effects of humidity and temperature on the strength*

The negative pore water pressure has been calculated using the pore size distributions obtained by the analysis of water-vapour desorption isotherms and the capillary model. How the strength varies with water content, void ratio and $e/\sqrt{S_r}$, (in which e is the void ratio and S_r the degree of saturation), under varying environmental conditions has been examined. The results reveal that e *vs* $\log q$ (in which q is the unconfined compressive strength) is a straight line for all soils during shrinkage. Even water content bears a similar relationship with q, a result which is in conformity with inferences from the rate-process theory[4]. The analysis of the effects of climate on stress-strain behaviour of soils has shown a unique relationship between unconfined compressive strength and initial tangent modulus for soils undergoing shrinkage.

4. Conclusions

The following main conclusions have been drawn based on the studies reported in the thesis:

1. In the presence of highly ligative organic molecules like DMSO and DMF, the clay behaviour can be explained by considering, in addition to the dielectric constant, the clay organic molecule interaction.
2. A non-dimensional modified free-swell index ($= V - V_s/V_s$) has been proposed to eliminate the inaccuracies found in Holtz and Gibbs' definition of free-swell percentage of IS code's definition of differential free-swell percentage. The proposed modified free-swell index bears unique relationship with liquid limit and oedometer per cent swell.
3. During shrinkage of soil under climatic influences, the pore-water tension depends not only on surface area but also on the pore-size distribution, the void ratio and the degree of saturation.
4. For soils undergoing shrinkage, there is a linear relationship between the void ratio and the log unconfined compression strength; also between the water content and the log unconfined compression strength.
5. While soils are undergoing shrinkage, there is a unique relationship between unconfined compressive strength and initial tangent modulus for all soils over the entire range of shrinkage from Proctor optimum conditions.

References

1. Sridharan, A. and Venkatappa Rao, G. — Mechanisms controlling the liquid limit of clays, *Proc. Istanbul Conf. Soil Mech. Foundn Engng*, 1975, Vol. 1, p. 75.
2. Holtz, W. G. and Gibbs, H. J. — Engineering properties of expansive clays, *Trans ASCE*, 1956, **121**, 641–677.
3. — *Code of practice on methods of tests for soils*, 1977, IS. 2720: Part (XL).
4. Mitchell, J. K. — The application of colloidal theory to the compressibility of clays, *Seminar on interparticle force in clay water-electrolyte system*, CSIRO, Melbourne, 1960, 2–97.

Thesis Abstract (M.Sc.(Engng))

Reliability studies of reinforced concrete members in flexure, shear and torsion by T. S. Srikanth.
Research supervisor: K. T. Sundara Raja Iyengar.
Department: Civil Engineering.

1. Introduction

A structure can be defined as an assembly of members proportioned to resist the design loads and it should satisfy the requirements of safety and serviceability. Safety may be defined as an acceptable degree of security against complete failure, which in concrete structures can occur by various modes such as axial compression, flexure, shear, torsion, etc. The serviceability requirement means that the member of structure should not in its life time deteriorate to such an extent that it fails to fulfill its functions for which it was designed.

Load and strength are uncertain in nature. These uncertainties have been taken into account by the use of partial safety factors in building codes. Until the advent of the limit state method, these partial safety factors were based on practical experience. It has now been found that many of these variables exhibit statistical regularity, which suggests that the theory of probability and statistics plays an important role in the selection of partial safety factors. In the limit state method the concept of probability and statistical methods are used to analyse the variations that occur in load and resistance. A structure is said to have reached a limit state when it is unsafe or ceases to perform its functions satisfactorily. Knowing the limit state, reliability of a structure can be defined as the ability to fulfill its design purpose or it is also defined as the probability that a structure will not reach its limit state during the specified reference period, which is taken as 50 years. A measure of structural reliability is usually expressed in terms of reliability index (β). Thus it is necessary that a reliability study is carried out in order to arrive at the proper values for partial safety factors or to check the adequacy of the partial safety factors given in a code. The latter aspect has been studied in this thesis in detail for reinforced concrete members designed as per the latest code[1], in flexure, shear and torsion.

2. Reliability analysis

Reliability analysis can be classified according to the type of approximations made and the ways in which reliability is defined. According to this, reliability analysis can be classified under three basic levels:

(i) *Level 3 method* which is the most complete method of reliability analysis. In this method, the probability of failure is determined, involving a multidimensional integration of the joint density functions over the safety domain. Its primary importance is in the field of research, for checking the validity of approximations and simplifications of the lower levels.
(ii) *Level 2 method* involves simple calculation in which safety checks are made at finite number of points of the safety domain. Random variables are characterized by the mean and variance with relevant distribution functions. Reliability is expressed in terms of suitable safety indices. The advanced first-order second-moment method[2] used in this thesis comes under this category.
(iii) *Level 1 method* is incorporated in the IS code[1]. Here safety is introduced into the structure by considering the characteristic load and characteristic strength which are multiplied/divided by partial safety factors to obtain design values.

3. Advanced first-order second-moment method[2]

This method is adopted on the present study of reliability analysis. If the resistance R and the load effect S are the only two variables occurring in the limit state equation, and if both R and S follow Gaussian distribution, the limit state function is linear in R and S, that is,

$$R - S = 0. \tag{1}$$

Defining a new variable

$$Y = R - S \tag{2}$$

with mean and standard equation as

$$\bar{Y} = \bar{R} - \bar{S} \tag{3}$$

and

$$\sigma_Y = [\sigma_R^2 + \sigma_S^2]^{\frac{1}{2}} \tag{4}$$

the reliability index (β) is defined by

$$\beta = \frac{\bar{Y}}{\sigma_Y} = \frac{\bar{R} - \bar{S}}{(\sigma_R^2 + \sigma_S^2)^{\frac{1}{2}}}. \tag{5}$$

The procedure used in determining β is given in ref. 2. Probability distributions of the variables involved as assumed in the calculation of β are given in Table I.

Table I
Probability distribution assumed in the calculation of β

Variable	Distribution assumed	Mean	Coefficient of variation	Reference
Dead load (D/D_n)	Normal	1.05	0.10	2
Live load (L/L_n)	Type 1 largest	1.38	0.25	2
f_{cu}(15 N/mm^2)	Log normal	23.57 N/mm^2	0.24	3
f_{SPR}(15 N/mm^2)	Normal	$0.53\bar{f}_c^{1/2}0.23[0.96 (1.238 + 0.11\log_{10} R1]$ N/mm^2	0.24	4
A_m/A_n	Truncated normal	0.99 (range 0.94 to ∞)	0.024	4
f_y(250 N/mm^2)	Normal	308.04 N/mm^2	0.102	computed
f_y(415 N/mm^2)	Normal	511.35 N/mm^2	0.102	computed
f_y(500 N/mm^2)	Log normal	511.42 N/mm^2	0.039	computed
df_{ys}	Normal	24 N/mm^2	0.134	4
a	Normal	Nominal	17.5 mm	4
b	Normal	Nominal + 2.4 mm	4.8 mm	4
d	Normal	Nominal − 4.8 mm	12.7 mm	4
Sv	Normal	Nominal	13.5 mm	4
Span	Normal	Nominal	17.5 mm	4

Note: For geometric quantities, standard deviations are given. $\bar{f}_c 0.23 = (0.54 f_{cu} + 7.58) \leq 0.92 f_{cu}$ N/mm^2.

3.1. *Evaluation of resistance*

For evaluating the member resistance in flexure, equations given in Indian Standards[1] are used after removing partial safety factors to arrive at the accurate strength prediction model. In the evaluation of resistance in shear, two shear-strength prediction models, *i.e.* of Patel[5] and Zsutty[6] were used. For evaluating the member resistance in torsion, two torsion-strength prediction models, *i.e.* Iyengar and Rangan model[7] and Hsu and Mo model[8] were used.

4. Summary and conclusions

Reliability index β has been calculated for reinforced concrete beams in flexure, shear and torsion. Extensive calculations have been done for three strengths of steel, *i.e.*, 250, 415 and 500 N/mm^2 and of concrete, *i.e.*, 15, 20 and 25 N/mm^2. From the results obtained, the following conclusions have been drawn:

(i) In flexure, β values increased with the increase in steel strength for the tension reinforcement, whereas in shear β values varied widely.
(ii) For beams in combined bending and torsion ultimately failing in flexure, there is an increase in the value of β when a higher strength tension steel is used. For torsion failures, β values are relatively high when a lower steel strength is used for stirrups.
(iii) To have a target reliability index β of 3.0 in flexure and 3.5 in shear and torsion, the live load factor in Indian Standards[1] needs to be changed to 1.8 from the existing value of 1.5.

References

1. *Indian Standard code of practice for plain and reinforced concrete*, IS: 456–1978.

2. Ellingwood, B., Galambos, T. V., MacGregor, J. G and Cornell, C. A. *Development of a probability based load criterion for American National Standard A 58, Building code requirements for minimum design loads in buildings and other structures*, Special Publication No. 577, National Bureau of Standards, Washington D.C., 1980, p. 228.

3. Ranganatham, R. and Dayaratnam, P. Statistical analysis of strength of concrete, *Bldg Environment*, 1976, **11**, 145–152.

4. Mirza, S. A. and MacGregor, J. G. Statistical study of shear strength of reinforced concrete slender beams, *ACI J.*, 1979, **76**, 1159–1177.

5. Patel, R. J. *Shear strength of reinforced concrete beams under uniformly distributed load*, M. E. Dissertation, Indian Institute of Science, Bangalore, 1977, p. 78.

6. Zsutty, T. Shear strength prediction for separate categories of simple beam tests, *ACI J. Proc.*, 1971, **68**, 138–143.

7. Sundara Raja Iyengar, K. T. and Vijaya Rangan, B. *Strength and stiffness of reinforced concrete beams under combined bending and torsion*, American Concrete Institute Publication, SP-18, 1968, pp. 403–440.

8. Thomas, T. C. H. and Mo, Y. L. Softening of concrete in torsional members—Design recommendations, *ACI J.*, 1985, **82**, 443–452.

Thesis Abstract (M.Sc.(Engng))

Thermomechanical deformation of rubber by K. S. Loganathan.
Research supervisor: Manas Chanda.
Department: Chemical Engineering.

1. Introduction

Heat build-up in rubber vulcanizates occurs as a result of rapid cyclic deformation of rubber. Rubber elasticity may be considered as very large deformability with almost complete recoverability. The ratio of the energy lost (*i.e.* converted to heat) to the energy recovered is the hysterisis. Heat build-up depends not only on the hysterisis of the rubber compound, but also on the thermal conductivity and the maximum thickness of the rubber specimen.

Strain-induced crystallisation, stress-softening, structure breakdown, deformation of domains in two-phase systems, and changes in network structure which decrease the elastic component, have all been cited by various authors[1,2] as the major sources of hysterisis in reinforced rubber compounds. Payne and Whittaker[3] listed the major sources of hysterisis in filled rubbers. Hysterisis is also dependent on the nature of polymers, crosslinking systems and fillers used in the compounding *i.e.* on the composition of the compound. However, these factors emerge with different degrees of importance in published literature as contributors to hysterisis, as each has been selectively studied, under test conditions which are not comparable. The objective of this work was therefore to compare the thermomechanical deformation of different practical rubber compounds under standardised test conditions and to analyse the major contributors to hysterisis.

2. Experimental programme

An internationally recognised compression (Goodrich) flexometer was chosen and the test conditions standardised at constant amplitude and oscillation frequency so that the effects of thermal failures and crosslink degradation due to environment and test conditions would be absent. Standards ASTM D 623, COST 266, DIN 53533 all describe methods of determination of heat build-up in this compression flexometer. The test involves applying a definite compressive load to a test piece through a lever system having high inertia, imposing on the sample an additional high-frequency cyclic compression of definite amplitude, and measuring with a thermocouple, the temperature rise at the base of the test piece.

The apparatus used for measuring the rheomatic properties was an oscillating disc curemeter, Monsanto R100S with microdie, $\pm 3°$ arc of oscillation, and at a temperature of 185°C. The trace of torque *vs* time generally defines the phases of vulcanisation-induction period, onset rate and time for optimum vulcanisation. Although it has not been established conclusively for all stages of vulcanisation, it is generally observed that the maximum torque value obtained on a rheometer is proportional to the degree of crosslinking of the rubber. The degradation of the network can also be studied by observing the time for reversion, *i.e.* for the maximum torque to fall by a definite amount with time.

A total of 107 practical rubber compounds of different compositions obtained from factory-mixed stocks were employed, the main variants in the composition being rubber, filler, compounding additives, vulcanising systems and separate rubber compounding ingredients. Rheometric properties which included minimum viscosity, scorch time, 90% cure time and maximum torque were measured for unvulcanised rubber compounds, while on vulcanised samples the temperature rise and compression set were measured using compression flexometer.

3. Main results and conclusion

The experimental and calculated data are analysed by correlating the temperature rise, compression set, and heat build-up with 13 different variables.

3.1. *Temperature rise, $\Delta T(^{\circ}C)$*

By multiple regression analysis, T is expressed in the form of equation:

$$\Delta T = 114.9104\phi' + 1.1062 \quad \text{(acetone extractables, by mass, \%)}$$
$$- 0.1927 \quad \text{(maximum torque, dN.M.)}$$
$$- 0.1518 \quad \text{(proportion of NR in the rubber, by mass)}$$

where ϕ' is the volume fraction of filler plus occluded rubber. The multiple correlation coefficient is 0.977.

3.2. *Compression set (%)*

A highly significant relationship, given below, is observed between the temperature rise ΔT and the compression set:

$$\Delta T = 2.0541 \quad \text{(compression set, \%)}$$

with a multiple correlation coefficient of 0.972.

The same four variables as above give a fair correlation with compression set, with a multiple correlation coefficient of 0.86.

It is observed that the deviations from the general relationship occur when the compression set is very low, as for example, in rubber compounds containing a hardening phenolic resin, and in compounds containing silica as filler.

3.3. *Heat build-up*

Heat build-up can be expressed in the form of equation:

$$Q = 125.260' + 2.467 \quad \text{(acetone extractables, by mass \%)}$$
$$- 0.271 \quad \text{(maximum torque, dN.M.)}$$
$$- 0.42 \quad \text{(proportion of NR in the rubber, by mass).}$$

The multiple correlation coefficient is 0.971.

It appears that the heat build-up in rubber compounds under compressive stress is largely dependent on its composition, *viz.*, the effective filler volume, and the proportion of low molecular mass species extractable by acetone. As both increase, the temperature rise increases. Among the four rubbers studied, natural rubber decreases ΔT, as also a high rheometer torque, which represents the degree of crosslinking. Of the four factors, the dominant one is the effective filler volume. This factor is also responsible as a 'strain amplification factor' for reinforcement. Thus a major factor for reinforcement is also the dominant factor for hysterisis. The presence of NR and of low molecular mass species, as well as crosslink density, are the other influences on hysterisis.

References

1. SABEY, B. E. — Skidding friction. The effect of hysterisis losses in tyre tread rubber, *Contemporary Phys.*, 1959, **1**, 56–61.

2. GILES, G. G. AND SABEY, B. E. — Rubber hysteresis and skidding resistance, *Engineering*, 1958, **186**, 840–842.

3 PAYNE, A R. AND WHITTAKER, R. E. — Importance of hysteresis in the reinforcement of elastomers, (J. B. Donnet, ed.) 1975, p. 233, CNRS.

Thesis Abstract (M.Sc.(Engng))

Chemical modification of epoxies [Studies on rubber toughening of epoxy resins using hydroxy-terminated poly (butadiene-co-acrylonitrile)] by S. Sankaran.
Research supervisors: Manas Chanda and R. Peravali (ADE).
Department: Chemical Engineering.

1. Introduction

Fracture toughened fibre reinforced composites and hence toughened matrix resins have become a necessary requirement in the structural design of aircraft components. Toughening of epoxy resins has drawn great attention in this context as they constitute a versatile class of materials to be used widely in fibre reinforced composite structures. A large number of publications have appeared[1–4] in which toughening of epoxy resin is accomplished through incorporating rubber resins in the epoxy matrix. However, liquid rubber CTBN [carboxy-terminated poly (butadiene-co-acrylonitrile)] is the only elastomer to be widely reported compared to others like HTBN [hydroxy-terminated poly (butadiene-co-acrylonitrile)], and generally the procedures described in the reports are based on the addition esterification reaction of CTBN with the epoxy resin. Quarternary ammonium or phosphonium salts and PPh_3 are used as catalysts. The possible reason for wide usage of CTBN seems to be the relative ease with which the carboxy function can react with the epoxy group under mild conditions thereby establishing chemical linkage with the epoxy matrix[5].

In this paper, an attempt has been made to toughen the epoxy matrix using HTBN and evaluate the extent of toughening along with other mechanical and thermal properties. The problem of chemically linking the elastomer is overcome by using toluene diisocyanate (TDI) as a coupling agent to link the elastomer HTBN and the epoxy forming a urethane linkage with the former and an oxazolidone ring with the latter.

2. Experimental

The synthesis of elastomer-modified epoxy resin was done in two stages (fig. 1). In the first stage the elastomer HTBN was reacted with TDI using laminating resin Araldite LY 556 (Hindustan Ciba-Geigy) as the reaction medium, at a temperature of 100–110°C to give isocyanate-terminated prepolymer in the reaction mixture. In the second stage, reaction of the prepolymer with the epoxy was carried out using tetra n-butyl ammonium iodide as the catalyst at a temperature of 145°C. The IR spectrum of the reaction mixture at the end of each stage was recorded and the epoxy values determined before and after chemical modification. The chemically modified epoxy resin was mixed with excess of LY 556 and cured with Hardener HT 972 (diamino diphenyl methane) to give cast

Table I
Mechanical properties of HTBN toughened epoxy formulation

Sl no	Formulation*	Ultimate tensile strength kg/sq. mm(mpa)	Tensile modulus kg/sq. mm(gpa)	Percentage elongation	Fluxural strength kg/sq. mm(mpa)	Toughness** kg/sq. mm(mpa)
1	EP-NEAT	6 92(67.88)	276.10(2.71)	3.48	8.02(78.6)	14.3(140.20)
2	EP-CRR-1.5	8.21(60.92)	304.25(2.98)	7.27	—	31.8(311.95)
3	EP-CRR-3.0	6.12(60.00)	430.30(4.22)	9.24	10.97(107.6)	49.1(481.66)
4	EP-CRR-6.0	5.19(50.91)	290.00(2.84)	8.62	8.34(81.8)	33.8(331.57)
5	EP-CRR-9.0	4.75(46.60)	234.70(2.30)	7.90	7.35(72.1)	30.0(294.29)
6	EP-CRR-12.0	4.10(40.22)	210.25(2.06)	10.00	3.82(37.4)	30.6(300.18)
7	EP-PBR-5.0	4.68(45.91)	287.28(2 82)	4.50	6.6(64.74)	16.1(157.94)

*EP stands for epoxy resin LY 556.
CRR stands for chemically reacted rubber, and
PBR stands for physically blended rubber.
**area under the stress-vs-strain curves.

epoxy specimens of elastomer content ranging from 0–12% (Table I for notations of different formulations). For comparison a cast specimen containing 5% HTBN was cast by physically blending the elastomer and curing. Ultimate tensile strength, tensile modulus were determined according to ISO R 527 and flexural strength as per ASTM D 790. The TG-DTA thermograms were recorded in both nitrogen atmosphere and in air. The morphology of the fractured resin surfaces were studied using scanning electron microscopy at magnifications of the order of 5000.

3. Results and discussion

The formation of urethane linkage in the preparation of prepolymer during first stage of the reaction derives support from the conspicuous reduction in the intensity of the broad peak centered around 3500 cm^{-1} (–OH stretching of HTBN and LY 556) and the appearence of a new peak at 3310 $^{-1}$ cm (–NH stretching) in the IR spectra of the reaction mixture after the first stage was over. The presence of isocyanate group (in the prepolymer) at this stage of the reaction is revealed by the band at 2270 cm^{-1} (–N=C=O stretching) which appears broad due to overlapping of the peak due to –C=N group (of HTBN). The same observation is confirmed by the emergence of peak at 2215 cm^{-1} with the characteristic shape that of –C=N of HTBN in the IR spectra of the reaction mixture after the second stage. An indirect evidence to the formation of oxazolidone is drawn from the change in shape and intensity of peak at 1730 cm^{-1}. The possible reaction scheme is given in fig. 1. Combined with these observations the epoxy values of the reaction mixture before and after chemical modification suggest that the hydroxyls of Araldite LY 556 also would have participated in the reaction.

The mechanical properties of the toughened epoxy formulations are given in Table I. Inclusion of HTBN in the epoxy matrix has generally improved toughness as measured by the area under stress-*vs*-strain curves. Rubber inclusion through chemical reactions up to 3% by weight has toughened the system without much reduction in the tensile strength while the tensile modulus has either marginally or substantially increased. The increase in the modulus can be attributed to an increase in the crosslink density resulting from the reaction of –OH group of the epoxy resin with the isocyanate of TDI, the other –NCO group of which would have got linked to epoxy group of yet another chain or molecule. The superiority of chemically linking the elastomer to epoxy matrix is brought out by a

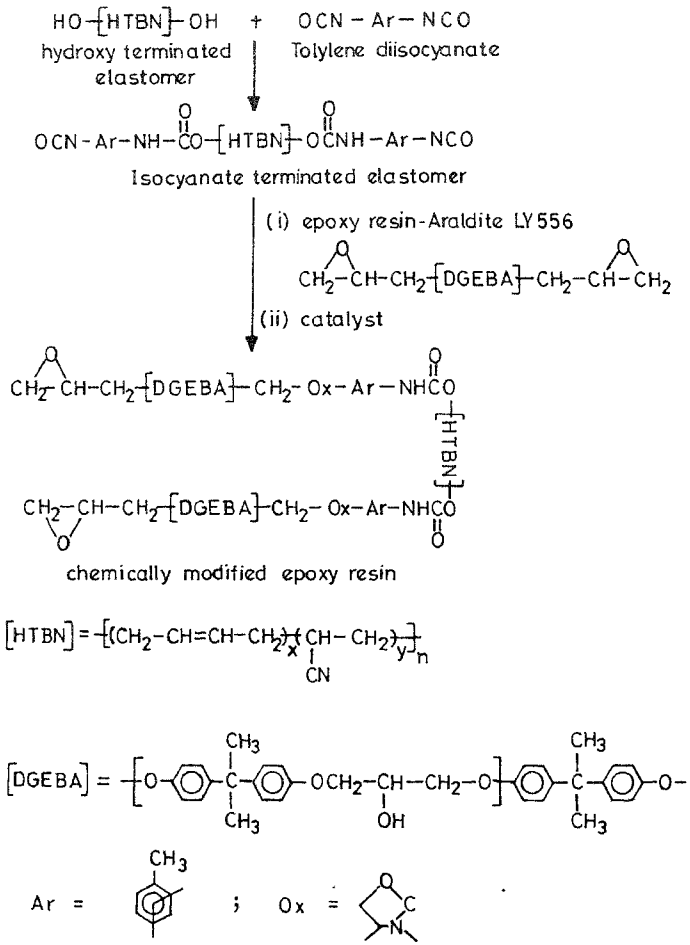

FIG. 1. Reaction scheme showing the formation of urethane and oxazolidone linkages during the chemical modification of epoxies.

comparison of the values of EP-PBR-5.0 with a near-similar situation in the case of chemically reacted rubber. The steep fall in ultimate tensile strength in the case of physically blended system will be a big disadvantage. The degree of improvement in the properties compare well with those reported[5,6] for the CTBN toughened ones.

The TG-DTA thermograms show that the *Tg* of HTBN toughened formulations (cured) are almost the same as that of the neat resin formulation, an indication that the thermal stability is retained without any deterioration. The TG thermograms in nitrogen are characterised by a steep degradation starting around 350°C and getting completed around 480–500°C. In air there are two degradation steps the first between 350 and 450°C and the second starting at 450°C. In both nitrogen and air the percentage weight loss (during the degradation step) for the rubber toughened formulations is slightly more than that of neat specimen. This may be due to high susceptibility of aliphatic chains of the rubber network in the molecular backbone for thermal and oxidative degradations.

The dual-phase morphology in the case of toughened epoxies is well brought out in the scanning electron micrographs of the fractured surfaces of the specimens. The soft rubber phase is precipitated from the hard epoxy phase during curing. The rubber particles act as crack stoppers during fracture, thereby producing multiple crack sites leading to toughening. The size distribution of the rubber particles becomes wider and the average particle size increases with the increasing percentage inclusion of the rubber (0.66 μm for EP-CRR-1.5 to 2.89 μm for EP-CRR-12.0). The number of rubber particles per sq mm shows a downward trend after an optimum concentration of the rubber (6%). It is inferred from these observations that a large number of smaller particles toughen the epoxies much better than a smaller number of larger particles. The range of particle sizes is much wider for the physically blended specimen and the number of particles per sq mm is much lower (10.3×10^3 for EP-PBR-5.0 compared to 67.2×10^3 for EP-CRR-6.0) confirming this point of view.

It can be concluded that chemically linking HTBN with the epoxies using TDI as a coupling agent holds good promise towards toughening the epoxies similar to CTBN.

References

1. SULTAN, J. N., LAIBLE, R. C. AND MCGARRY, F. J. — *Appl. Polym. Symposia*, 1971, **16**, 127–136.
2. ROWE, E. H., SIEBERT, A. R. AND DRAKE, R. S. — *Mod. Plast.*, 1970, **47**, 110–112.
3. PAUL, N. C., RICHARDS, D. H. AND THOMPSON, D. — *Polymer*, 1977, **18**, 945–950.
4. BASCOM, W. D., BITNER, J. L. AND MOULTON, R. J. — *Composites*, 1980, **1**, 9–18.
5. RIEW, C. K., ROWE, E. H. AND SIEBERT, A. R. — *Toughness and brittleness in plastics*, Advances in Chem. Series No. 154, Am. Chem. Soc., 1976, p. 326.
6. MEEKS, A. C. — *Polymer*, 1974, **15**, 675–680.

Thesis Abstract (M.Sc.(Engng))

Investigations on gas-liquid ejector by P. T. Raghuram.
Research supervisors: R. Kumar and T. R. Das.
Department: Chemical Engineering.

1. Introduction

Studies have been made on a gas-liquid contacting device which offers a high interfacial area and better mass transfer coefficient. A survey has been made for various gas-liquid contactors offering different range of interfacial area[1]. It has been observed that ejectors are one of the best conventional contactors for gas-liquid systems.

The study on the ejector has been made as it offers an adjustable contacting time and cocurrent flow for high interfacial area. An ejector has been fabricated out of glass and the reacting system selected for the study is carbon dioxide (air–carbon dioxide mixture)–sodium hydroxide solution.

2. Principle

The ejector essentially consists of a small nozzle and a suction tube. Sodium hydroxide solution has been pumped through this nozzle and lean carbon dioxide gas has been sent through the suction line. A gas-liquid dispersion has been generated in the mixing section of the ejector[2]. A turbulent mixing is observed in this section with very fine bubble formation. The bubble size grows quickly in the diverging section of the ejector as it moves downwards and the dispersion leaves the ejector through the uniform diameter tube of the exit column.

The work intended is to model the performance of an ejector contactor for the chemcical system used. As the bubble coalescence and mixing phenomena are highly complex, the bubble size has been obtained through experiments and simplified assumptions. A model has been proposed for the pseudo first-order kinetics in the fast reaction regime.

3. Experimental set-up

The experimental set-up mainly consists of a HDPE tank to store sodium hydroxide solution with stainless steel baffles and a centrifugal pump. Measured amount of liquid is pumped through rotameter to the main nozzle of the ejector. A bypass line from the pump extends into the tank to recirculate the solution for better mixing.

Carbon dioxide gas and air at known flow rate are mixed in a glass chamber and sent through the secondary line of the ejector at a slightly positive pressure. A gas-liquid dispersion generates in the mixing chamber of the ejector and moves down through the uniform diameter tube of the ejector and is collected into another tank. Samples have been collected at the inlet and outlet of the ejector for estimating the amount reacted.

Experiments have been carried out with different column lengths of the ejector using different gas-liquid parameters such as gas and liquid concentrations and liquid flow rates to observe their effect on conversion.

A stable dispersion has been generated in the ejector under the following experimental conditions:

Liquid flow rate : 75.2 to 131.6 cm^3/s
Gas flow rate : 50.8 and 65.1 cm^3/s

Liquid
concentration : 0.1 to 0.5 N
Gas concentration : $0.1035–0.182 \times 10^{-4}$ g mol/cm^3
Column length : 6.2, 16.1, 26.5 and 35.7 cm.

4. Modelling

A preliminary model which has to depend on some measured parameters has been proposed for the performance of the ejector for gas-liquid reacting system. The proposed model considers the ejector as a contactor with a series of stirred vessel reactors followed by a plug-flow reactor. The ejector has been considered to be divided into four sections: jet, dispersion, coalescence, and uniform flow sections.

Stirred vessel model assumptions have been made for the first three sections whereas the plug flow model analysis has been applied for the last section. Bubble size at different sections of the ejector has been estimated using interpolating values from experimental data and theoretical estimations available from the existing Sprow's correlation[3]. Gas hold-up has been assumed to be the same throughout for this relatively non-coalescing system and values have been calculated from the gas and liquid feed data. The reaction for the system chosen is controlled by the liquid film and mass transport accompanied by fast chemical reaction proceeds as the two phases move down along the contactor.

5. Results and discussion

The conversion increases when either the liquid flow rate, the gas concentration, or the liquid concentration to the system is increased. The length of the uniform cross section tube of the ejector also improves the conversion, as the length increases.

The results obtained through the model are in good agreement with the experimentally determined values of conversion. The model also shows there is an improvement in conversion as a result of increase in the above parameters. The model not only predicts the general trends but also gives correct values of the resulting conversions. This analysis can be used as the starting point for developing more robust models.

References

1. Coulson, J. M. and Richardson, J. F. — *Chemical Engineering*, 1971, p. 82, Pergamon.

2. Reddy, Y. R. and Kar, S. — Theory and performance of water jet pump, *J. Hydraulics Div., ASCE*, 1968, **94**, 1261–1281.

3. Sprow, F. B. — Distribution of drop sizes produced in turbulent liquid–liquid dispersion, *Chem. Engng Sci.*, 1967, **22**, 435–442.

Thesis Abstract (M.Sc.(Engng))

Scaled model studies of sloshing and its suppression in propellant tanks of a launch vehicle by J. V. Kamesh.
Research supervisor: S. Durvasula.
Department: Aerospace Engineering.

1. Introduction

The sloshing motion of a liquid is quite a commonplace occurrence. Liquids with a free surface are quite easily set into large amplitude oscillations, which results in substantial lateral forces on the container. Lateral sloshing of the liquid is the most important amongst the various types of dynamic behaviour of the liquid and has, consequently, been the subject of extensive study–analytically as well as experimentally[1]. Thus, it can be readily perceived that the phenomenon indeed becomes very important in the context of large liquid propelled launch vehicles, like the Polar Satellite Launch Vehicle (PSLV), from the point of view of avoiding undesirable interaction between liquid sloshing, overall body bending and the dynamics of control system to ensure that the vehicle follows the intended flight trajectory.

In PSLV, which is a four-stage launch vehicle, the second stage (PS2) is propelled by liquid propellants–unsymmetrical dimethyl hydrazine (UDMH) being the fuel and nitrogen tetroxide (N_2O_4) being the oxidiser. In the present study, scaled models of the fuel and oxidiser tanks made of perspex, which are geometrically similar to the prototype tanks, are used to study the phenomenon. These tanks are cylindrical in shape with torospherical ends. The main aim of this study was to determine the forces and moments caused by the sloshing liquid for various liquid heights (simulating the continuously depleting propellant in the prototype) to formulate a mathematical model to represent the phenomenon for use in the structure-control interaction studies. In addition, effective prevention of slosh at full liquid height by the use of an optimally located annular ring baffle was also examined.

2. Experimental

The philosophy behind the experiment has been derived from the well-known dynamic similarity considerations which postulate the theorem of dynamic similitude. The two non-dimensional π terms relevant to the present study are $F/\rho g D^3$ and $w\sqrt{D/g}$.

The first set of experiments were done using 1/10 th scale tanks. They were suspended in a pendular fashion and oscillated by the use of an electrodynamic exciter. The results provided an idea of the slosh force levels and the natural frequencies for various liquid heights. These results helped in all aspects of design and fabrication of the 1/5 th scale tanks using which the most important phase of the entire experimental study was conducted.

A test rig consisting of a nearly friction-less vibration table driven by a 10 HP induction motor coupled to an eddy-current variable speed unit was designed and commissioned for this study. The two 1/5 th scale tanks were mounted successively on this moving platform and the experiments conducted. In this phenomenon, the first mode is very dominant and the slosh force corresponding to it far outweighs that due to other modes. So, the effort was mainly concentrated on determining the slosh force, vertical reaction due to the moving liquid, natural frequency and slosh amplitude corresponding to the fundamental mode. Figure 1 shows the typical first mode shape. The need for a baffle near the free surface of the liquid may be readily appreciated.

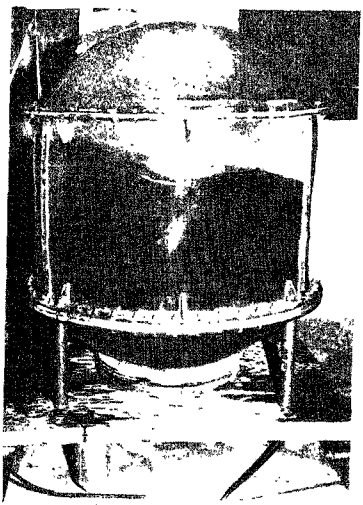

FIG. 1. First mode shape of sloshing in $\frac{1}{3}$th scale model of oxidiser tank (unbaffled).

Subsequently, all the acquired data are used in arriving at the parameters of the two traditional mathematical models in the form of simple pendulum as well as spring-mass system. This is done by using a system of four equations formulated as a part of this work[2].

3. Results

Figure 2(a) shows the magnitude of forces that could occur at resonance. As the liquid height depletes, slosh forces also reduce. The narrow peaks indicate the low damping provided by the tank walls– Damping ratio $\gamma = 0.6\%$, while the maximum slosh force, as a non-dimensional parameter $F/\rho g D^3 (x_0/D) = 27$. However, the introduction of a baffle just below the liquid's free surface has reduced the force level to 7 at resonance and γ has increased very substantially to 10–12% (fig. 2(b)).

The slosh force data have been reduced to yield the sloshing mass, m_1, non-sloshing mass, m_0, their locations with respect to the free surface of the liquid, pendulum length, l_1, and spring constant k_1. These values derived from experiments in a right circular cylinder are compared with the analytical results available[3] and the agreement was found to be good, thereby validating the experimental procedure for the PSLV tanks also with torospherical bottom.

In this study, the efficacy of the novel concept of a low pitch, helical baffle, was also investigated. The helical baffle's effect is felt, as may be envisaged, over a larger range of liquid depths. Normally, a series of ring baffles spaced apart suitably along the height are often used which involves considerable

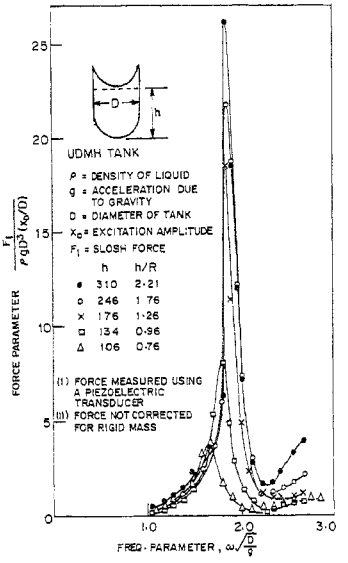

FIG 2(a). UDMH tank unbaffled

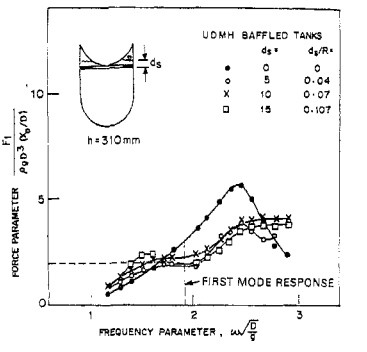

FIG 2(b). UDMH tank baffled.

weight penalty. The results of the study on helical baffle confirm that the efficacy of this baffle configuration is maintained over a wide range of liquid heights, though the magnitude of damping is slightly lower than that of an optimally located ring baffle[4]. Another advantage is that it would be effective even for inclined orientations of the tank as would happen when the vehicle is on its flight trajectory.

Nomenclature

D : Diameter of tank,
F : Slosh force,
g : Acceleration field,
X_0 : Displacement,
ρ : Density of the fluid,
w : Circular frequency,
γ : Damping ratio.

References

1. ABRAMSON, H. N. *The dynamic behaviour of liquids in moving containers*, NASA SP-106, 1966.

2. KAMESH, J. V AND DURVASULA, S. Model parameters derived from small amplitude excitation, presented at the *Fourth Inhouse Seminar on Space Science and Technology*, 29th July 1987, ISRO-IISc Space Technology Cell, Indian Institute of Science, Bangalore.

3. *Propellant slosh loads, NASA space vehicle design criteria (Structures)*, NASA SP-8009, 1968.

4 DURVASULA, S. AND KAMESH, J. V Model investigation of the novel concept of a helical baffle for suppression of liquid sloshing in propellant tanks, Paper presented at the Technical Sessions of the *38th Meeting of the Aeronautical Society of India*, NAL, Bangalore, Dec. 1986.

Thesis Abstract (M.Sc.(Engng))

Some studies concerning flow-induced structural noise of a sonar dome by V. Bhujanga Rao.
Research supervisors: M. L. Munjal and N. K. Ramanarasaiah (Orgn).
Department: Mechanical Engineering.

1. Introduction

A wide range of ships such as research vessels, fishing craft, survey vessels and warships are provided with sound navigation and ranging (SONAR) systems for various applications. The transducers of these sonars are mounted inside free-flooding streamlined bodies called sonar domes. The sonar transducers mounted inside these domes are operated in a certain frequency range. Generally the environment in which it is operated on board any ship is noisy. That part of ship's noise which goes and interferes with the sonar in the band width of sonar operating frequency is called self-noise of the sonar. In any ship's sonar systems the main sources of self-noise operating simultaneously are: i) machinery-excited noise; ii) flow-excited noise; iii) propeller-excited noise.

The present investigation pertains to flow-excited noise of sonar dome in the generation of sonar self-noise.

There are two major sources of flow-excited noise of sonar dome *viz*., cavitation and eddying. Cavitation of sonar domes may be avoided, throughout the speed range of the fastest vessels, by proper choice of form and length diameter ratio while it is very difficult to overcome eddying problem. In the case of sonar domes which are basically streamlined bodies, turbulent flow over the surface of the dome occurs for two reasons.

i) The dome is generally located in that part of the ship's hull where the flow is highly disturbed and also turbulent.
ii) Though the surface finish of the wall is smooth at the time of installation, with passage of time marine fouling occurs and the surface becomes rough leading to turbulent flow.

In turbulent flow, boundary layer pressure fluctuations cause both flow noise and flow-induced structural noise. Flow noise is defined as the noise that is produced by the hydrodynamic flow around a rigid body and in general encompasses all those phenomenon in which unsteady flow fields induce pressure fluctuations. Apart from flow noise, there is another mechanism which is found to be dominant source of self-noise in the case of sonar domes. That is, eddies in turbulent flow excite the dome wall into flexural vibrations which radiate noise into the interior of the dome. This can be called the flow-induced structural noise in order to clearly distinguish it from the flow-noise phenomenon.

The theory and analysis of the flow-induced structural noise of sonar dome is an interesting, albeit specialised problem, requiring for its solution a blend of hydrodynamics, structural dynamics, vibro-acoustics and fluid structural interaction modelling techniques.

2. Experimental and analytical studies

In the present investigation, experimental as well as analytical studies were carried out for understanding the importance of the flow-induced structural noise as a source of self-noise.

As a first step to estimate the turbulent pressure fluctuation amplitude as input function, the hydrodynamic characteristics of a typical sonar dome such as potential flow pressure distribution, velocity distribution, boundary-layer characteristics were evaluated.

The turbulent wall pressure cross-spectral density function given by Corcos[1,2] and turbulent wall pressure auto-spectral density function given by Skudyrzk and Haddle[3] have been found to be in good agreement with the available experimental results and therefore used in this thesis for mathematical modelling of the input turbulent pressure fluctuations.

When the prescribed forces are known, it becomes an elastic problem to calculate the response of the dome-wall vibrations. The vibration response of dome wall as an idealized plate with simply supported boundary conditions was estimated using Strawderman's expressions[4].

In a domed sonar system, the importance of flow-induced structural noise of dome wall as a source of sonar self-noise depends on the intensity of the other noise-producing sources and their generating mechanism on board any ship. Some shipboard experimental studies have been carried out in order to establish various dominant sources of self-noise and to ascertain relative importance of flow-induced structural noise of dome wall.

Besides analytical prediction of dome-wall vibration due to turbulent boundary-layer flow excitation, prediction of flow-induced structural noise levels in the interior of the dome is considered important. It may be pointed out that the dome is not really a reverberant chamber and account should be taken of shadowing and directivity effects associated with large sonar arrays that occupy a significant fraction of the dome volume. In order to overcome some of these problems, a semi-analytical and semi-experimental method is proposed for predicting the flow-induced structural noise in the laboratory acoustic tank with any prototype model of the dome.

References

1. Corcos, G. M. — Resolution of pressure in turbulence, *J. Acoust. Soc. Am.*, 1963, **35**, 192–199.
2. Corcos, G. M. — The structure of the turbulent pressure field in boundary-layer flows, *J. Fluid Mech.*, 1964, **18**, 353–378.
3. Skudyrzk, E. K. and Haddle, G. P. — Noise production in a turbulent boundary layer by smooth and rough surfaces, *J. Acoust. Soc. Am.*, 1960, **32**, 19–34.
4. Strawderman, W. A. and Brand, R. S. — Turbulent-flow-excited vibration of a simply supported, rectangular flat plate, *J. Acoust. Soc. Am.*, 1969, **45**, 177–192.

Thesis Abstract (M.Sc.(Engng))

Allocation of skilled assembly manpower under proportionality restrictions by G. Karthikeyan.
Research supervisor: K. N. Krishnaswamy.
Department: Management Studies.

1. Introduction

Allocation of manpower to the production of assemblies and that to components can generally be treated by similar modelling techniques like assignment and transportation algorithms[1,2]. But there are situations in which the allocation to assembly operations may become more complex. General linear programming can be used with advantage in such cases.

2. Allocation of manpower to assembly operations

In several situations manpower allocation is required to component production so that the assembly demand forecast is met and inventories of components are not permitted. Storing of certain kinds of sub-assemblies over a period of time makes it unsafe. In general, there may be quite a number of operations needed to be performed to produce one assembly. Further some production systems may require that the number of sub-assembly items to meet the demand on the assembly be performed in such a way as to leave no inventory of sub-assemblies. Thus the matching of components/sub-assemblies will have to be explicitly considered in the allocation procedure for component/sub-assembly production itself. Some features of the problem are:

a) A set of workers, in general, can perform an operation and a worker can perform several different operations. Among these a few workers are very versatile and can perform a wide variety of operations. However, certain operations can be performed by only one worker though every worker can perform more than one operation. This makes some operations more critical than the others.
b) Imbalances exist simultaneously in manpower in certain categories and in the work load on certain operations. That is excesses in certain skills and shortages in others, excess load in certain operations and shortage in others.
c) The sub-assemblies are non-inventoriable. It follows that the number of sub-assemblies produced are to match exactly the requirements of the number of assemblies to be produced, or be in exact proportion to each other sub-assemblies going into the assembly.

The above problem having very special requirement and constraints was observed to be new, not covered in the literature. The study of the problem therefore was taken up with an objective to develop a manpower allocation procedure such that: i) the utilisation of the skilled manpower in the shop is maximized: ii) urgent orders of short notice to the shop are honoured, thereby gaining customer good will; iii) a practical procedure reliable enough for use and easily understandable is evolved.

3. General linear program for the problem

The general linear programming model for the situation is as follows:

Maximize

$$\sum_{i}\sum_{j}\sum_{kj} X_{ijkj}$$

subject to

$$\sum_j \sum_{k_j} X_{i,jk_j} \leq ii_j, \quad \text{for all } i\text{—manhours available} \tag{1}$$

$$\sum_{k_j} X_{i,jk_j} \leq p_j r_{jk_j}, \quad \text{for all } k_j\text{—forecast quantities in manhours} \tag{2}$$

$$\sum_i X_{i,jk_j} - r_{jk_j} \sum_j \sum_{k_j} X_{i,jk_j} = 0, \quad \text{for all } k_j \forall j - \text{proportionality constraint} \tag{3}$$

$$X_{i,jk_j} \leq 0$$

where X_{i,jk_j} is the decision variable representing the manhours required by the *ith* operator to perform the k_jth sub-assembly operation belonging to the *jth* assembly.

The problem was first formulated as a linear program and solved. A special set of constraints termed 'proportionality constraints' were introduced in the linear program to satisfy the requirements of the non-inventoriable condition of the sub-assemblies[3]. The solution to the LP model gave the optimal allocation of manhours of each worker to individual sub-assembly operation of an assembly.

Several useful inferences were obtained from this solution. Range analysis performed, indicated that the system is highly sensitive to manhours demanded. This could be quite useful in designing an optimal manpower system.

4. Heuristic model and validation experiments

A heuristic procedure[4] was developed for the same problem more as an exploration and extension of the thumb rules of the shop managers. Three priority indices were developed for use in the heuristic procedure. They were termed, (i) versatility index, (ii) flexibility index, and (iii) sub-assembly index. Using these three indices and other heuristic rules a heuristic program in FORTRAN and Pascal was developed and run on DEC-1090 computer system. The heuristic procedure was attempted to be validated using (a) comparison with LP allocation, and (b) CPU times for processing.

5. Main results and conclusions

The heuristic procedure developed for the problem has the main advantage over LP of obtaining integer values for components produced. This may be a better approach when production quantities are small and integer results are desirable. The results at a glance:

I. Assemblies completed

Method	Forecast quantity	Completed quantity	Off-loaded quantity
LP	938.25(100%)	843.71(89.92%)	94.43(10.07%)
Heuristic	938.25(100%)	802.00(85.47%)	136.25(14.52%)

II. Manhours utilized

Method	Manhours available	Manhours allocated	Manhours Unallocated
LP	828(100%)	828(100%)	
Heuristic	828(100%)	564.19(68.13)	263.81(31.86%)

It is believed that this study has dealt with a special class of manpower allocation problems not dealt with hitherto and is a contribution to the field. Other possible formulations outlined in the thesis indicate potential for further research in this area.

References

1. APPA, G M. The transportation problem and its variants, *Operations Res. Q*., 1973, **24**, 79–82.
2. KAHALAS, H. AND GRAY, D. A. A quantitative model for manpower decision making, *Omega*, 1976, **4**, 17–24.
3. MULLER-MERBACH, H. Heuristics and their design: A survey, *Eur. J. Operation Res.*, 1981, **8**, 1–23.
4. ROTHBLUM, U. G. On solving optimisation problems with proportion constraints, *Math. Progm.*, 1978, **15**, 77–86.